Distribution Category:
Coal-Based Materials and
Components (UC-114)

ANL/FE--92/1

DE92 017143

ARGONNE NATIONAL LABORATORY
9700 South Cass Avenue, Argonne, Illinois 60439

ANL/FE–92/1

OXIDATION BEHAVIOR OF IRON–CHROMIUM ALLOYS AT ELEVATED TEMPERATURES: A REACTIVE–ELEMENT EFFECT

by

J.-H. Park and K. Natesan

Materials and Components Technology Division

March 1992

Work sponsored by
U.S. DEPARTMENT OF ENERGY
Office of Fossil Energy, Advanced Research and Technology Development Materials Program,
Work Breakdown Structure Element ANL-3

CONTENTS

FIGURES

TABLES

OXIDATION BEHAVIOR OF IRON–CHROMIUM ALLOYS AT ELEVATED TEMPERATURES: A REACTIVE–ELEMENT EFFECT

by

J.–H. Park and K. Natesan

ABSTRACT

Oxidation tests were conducted on samples of Fe-25Cr, Fe-25Cr-0.3-1.0Y, and Fe-25Cr-1Ce at temperatures of 700 to 1000°C and oxygen partial pressures of 1 to 20 atm for time periods of 19 to 160 h. In some tests, oxidized samples were quenched from test temperature to room temperature in ≈20 min to examine characteristics of the spallation scales. The results showed that the scales, even though of the same composition, spalled totally when developed on Fe-25Cr alloy, while those on Ce- and Y-containing alloys exhibited good scale adherence and no spallation. After removal of the spalled scales, specimens of Fe-25Cr alloy were reoxidized to gain insight into development and morphology of thermally grown scales and their spallation characteristics. The reoxidized samples formed complex scale layers that had iron oxide phase at the gas side of the interface; the scale layer was adherent and no spallation was noted. Experiments were conducted to evaluate the roles of alloy grain size and grain growth rate in development and spallation of oxide scales. Results showed that excessive alloy grain growth is the primary cause of spallation of thermally grown scales. Additions of reactive elements such as Y and Ce minimize alloy grain growth and thus improve the adhesion of scales to the substrate and virtually eliminate spallation.

INTRODUCTION

Corrosion resistance of a number of structural alloys in high-temperature environments is achieved by the formation of a continuous chromium oxide (Cr_2O_3) scale.[1,2] The scale can be treated principally as a rate-determining solid-state diffusion barrier between the environment and the alloy substrates. Research on high–temperature oxidation of structural alloys has two basic objectives: determining alloying additions to reduce the rate of oxidation, and improving adhesion of the oxide scale to the substrate alloy.[3] It is generally recognized that when alloys contain so–called reactive elements (sometimes known as oxygen–active elements), i.e, yttrium, lanthanum, cerium, etc., they exhibit a lower growth rate of the oxide and enhanced adhesion of the oxide layer to the base alloy.[4] Research on reactive–element additions has two main objectives: slowing the ionic transport rate through the scale, and increasing the degree of scale adhesion to the base alloy.

The objective of the study described here is to evaluate the oxidation behavior of chromia-forming alloys of Fe-25Cr base composition with and without additions of reactive elements. Alloys with Y and Ce additions in a range of 0.1-1.0 wt.% were used to determine the nature of the reactive–element effect on high–temperature oxidation. Thermogravimetric analysis (TGA) and postexposure microscopic examinations were conducted on samples prepared by thermal oxidation of chromium and Fe-25Cr alloys with and without additions of reactive elements The evaluation of oxidation kinetics included detailed analyses of scale–spalling characteristics and the substrate alloy grain growth that occurs during oxidation.

EXPERIMENTAL PROCEDURE

Thermogravimetric Measurements

The oxidation experiments were performed with an electrobalance (made by CAHN Instruments, Inc.) that had a sample capacity of 2.5 g and a sensitivity of 0.1 μg. The weighing mechanism was enclosed in glass assemblies that isolated the reaction gas mixture from the balance mechanism. The reaction chamber was connected to the balance assembly by a quartz tube. The furnace consisted of three-zone Kanthal heating elements with a temperature capability of 1200°C in continuous operation.

The test specimens were suspended from the balance with an ≈200-μm-diameter platinum wire. The tests were started by setting up the specimen at room temperature and purging the system with the appropriate reaction gas mixture. The specimen was heated in the reaction gas to the desired test temperature, and changes in sample weight were monitored continuously. Upon completion of the test, the furnace was opened and the specimen was cooled rapidly in the reaction gas environment. Oxidation tests were conducted at temperatures between 700 and 1000°C in oxygen, air, 1 vol% CO-CO_2, and 18 vol.% CO-CO_2 environments. Table 1 lists the specimens tested under various conditions, along with exposure times. A majority of the tests were conducted with Fe-25Cr and Fe-25Cr-0.3Y alloys. However, some tests were conducted in O_2-N_2 gas mixtures (with an oxygen partial pressure [pO_2] of 10^{-4} atm) at 1000°C on Fe-25Cr alloys containing1.0 wt.% Y or Ce.

Alloy Grain–Growth Tests

Specimens of Fe-25Cr, Fe-25Cr-1Y, and Fe-25Cr-1Ce alloys were used in tests to evaluate the role of alloy grain growth on the adhesion properties of thermally formed scales with substrate alloys. The specimens were tested at 1000°C for <1 to 24 h. The specimens were wrapped in tantalum foil (which served as an oxygen getter) and enclosed in quartz capsules under vacuum. The microstructures of the annealed specimens were examined by optical microscopy and scanning electron microscopy (SEM). In addition, large–grain specimens of Fe-25Cr (annealed at 1000°C for ≈25 h) were oxidized in TGA tests similar to those described earlier.

Electrical Resistivity Measurements

Foil samples of Fe-25Cr and Fe-25Cr-1Ce alloys were used to evaluate the role of reactive elements and oxidation in the electrical conductivity of the oxide scales. Foil samples of the two alloys were prepared by arc melting in an inert atmosphere. The alloys were rolled into sheets, wrapped in Ta foil, and vacuum-annealed at a pressure of $<10^{-5}$ torr; they were then heated to 1050°C, held at that temperature for 15 min, and furnace-cooled. The alloys were then individually cold-rolled to a thickness of 0.375 mm. After each foil sample was reduced to a thickness of 25 μm by repeated heat treatment and cold-rolling, it was given a final anneal.

Foil samples of Fe-25Cr and Fe-25Cr-1Ce alloys were mechanically polished and cut into a rectangular shape (8.9 x 16.5 x 0.05 mm) for use in a four-probe electrical-conductivity measurement. Details on the conductivity cell have been described elsewhere.[5,6] The electrical leads were 125-μm-thick Pt wires wrapped around the foil and spot-welded. The alloy samples were oxidized in a flowing gas mixture of N_2 and O_2 by connecting the samples in series and passing an electrical current through them. The samples were oxidized at 1083°C in a gas mixture of $pO_2 = 10^{-4}$ atm, and the temperature was subsequently lowered to 714°C by flow of inert gas. TGA tests were also conducted on the foil samples of the alloys for comparison with data on thicker specimens.

Electrical conductivity was measured by a standard four-probe method at a fixed DC current from a Keithley Calibrator/Source Model 263 over a range of 10-100 μA. We observed no appreciable differences that could be attributed to polarization in the DC measurement at the temperatures of this study. Sample surfaces and fracture edges were examined by SEM.

RESULTS AND DISCUSSION

Oxidation of Fe-25Cr and Fe-25Cr-0.3Y Alloys

Fe-25Cr

Figure 1 shows the calculated values for equilibrium pO_2 for several of the gas mixtures used in this study. Also shown in the figure are the pO_2 values for Fe/FeO and Cr/Cr_2O_3 equilibria, calculated from thermodynamic data on metal oxides. Figure 2 shows the thermodynamic stability regions for various iron oxides as a function of temperature and pO_2.[7] Table 1 lists specimen numbers and exposure times (which were 40–160 h) used in the oxidation tests. Figure 3 shows the sample surface oxidized at 1000°C in 1 vol.% $CO-CO_2$ for 70 hr. Convoluted oxide in (a), iron oxide in the edge region of the sample (b), and an area of spalled oxide in (c) are evident. Based on the thermodynamic stability data shown in Fig. 2, formation of any of the three iron oxides is possible in the exposure environment. The formation of only iron oxides in the edge regions of the sample (see Fig. 3b) indicates that Fe diffusivity is much faster in the stressed areas of the sample. Once the iron oxide forms, by virtue of the higher diffusivity of Fe (than of Cr) in iron oxide,[8-13] chromium oxide rarely forms in those regions. The ratio of Fe to Cr diffusivity can be estimated to be 1×10^4 to 4.5×10^4, based on a comparison of observed grain sizes of the oxides of Fe and Cr. The flat regions of the sample showed predominantly chromium oxide, even though it was prone to spallation.

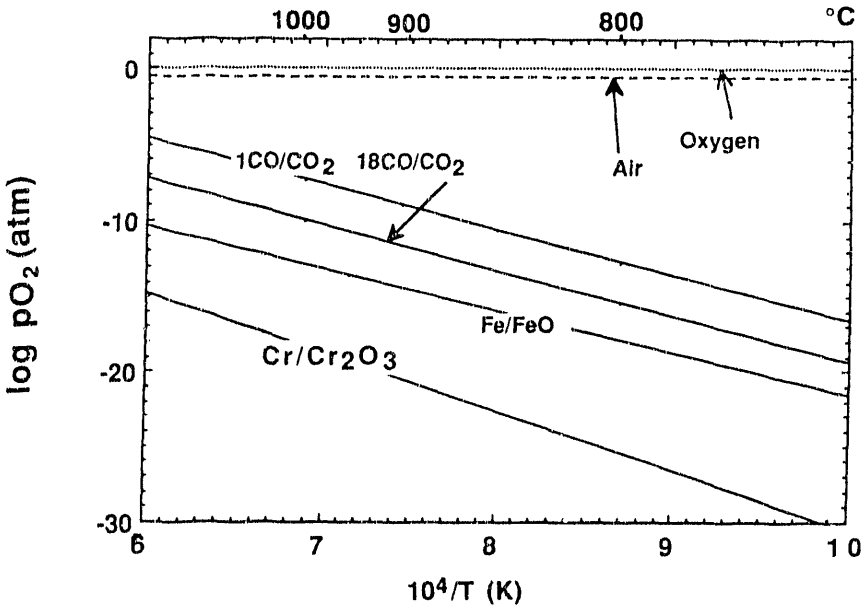

Fig. 1. Temperature dependence of oxygen partial pressure for several gas mixtures and metal/metal oxide systems

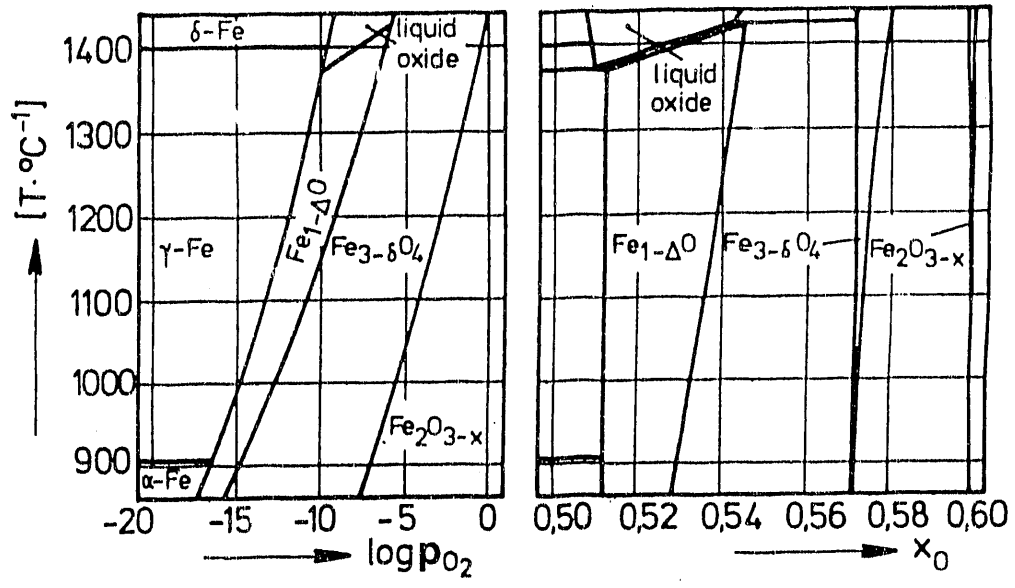

Fig. 2. Phase stability diagram for Fe–O system

Table 1. Sample identification and exposure times (h) for various TGA tests[a]

Alloy and Environment	1000°C	900°C	800°C	700°C
Fe-25Cr				
Oxygen	FC-2 (94)	FC-1 (92)	FC-11 (135)	FC-51 (160)
Air	FC-5 (40)	FC-22 (90)	FC-16 (90)	FC-3 (130)
1%CO-CO_2	FC-4 (70)	FC-8 (90)	FC-14 (140)	FC-12 (110)
18%CO-CO_2	FC-88 (120)	FC-2 (138)	FC-10 (115)	FC-17 (67)
Fe-25Cr-0.3Y				
Oxygen	FCY-3 (120)	FCY-7 (98)	FCY-0 (90)	FCY-1 (90)
Air	FCY-8 (74)	FCY-26 (84)	FCY-2 (90)	FCY-11 (115)
1%CO-CO_2	FCY-22 (70)	FCY-6 (86)	FCY-4 (120)	FCY-33 (110)
18%CO-CO_2	FCY-21 (119)	FCY-77 (138)	FCY-24 (115)	FCY-66 (67)

[a]FC-# and FCY-# indicate Fe-25Cr and Fe-25Cr-0.3Y alloys, and numbers in parentheses indicate exposure times in hours.

Figure 4 shows SEM photomicrographs of Fe-25Cr alloy specimens exposed at 900°C to different oxidizing environments. The specimen developed coarse–grain oxide in O_2, somewhat smaller–grain oxide in air and 1 vol.% CO-CO_2 gas, and a fine–grain oxide in 18 vol.% CO-CO_2 gas. The oxide scales that developed in air and 1 vol.% CO-CO_2 gas mixture were prone to spallation that can be attributed to the presence of Fe in the scale; this indicates that Fe transport (a dominant feature at higher oxygen pressures) is a primary cause of scale spallation. The scale that developed in 18 vol.% CO-CO_2 gas did not contain Fe, and virtually no spallation of scale was noted. Figures 5 and 6 show SEM photomicrographs of surfaces of Fe-25Cr alloy specimens

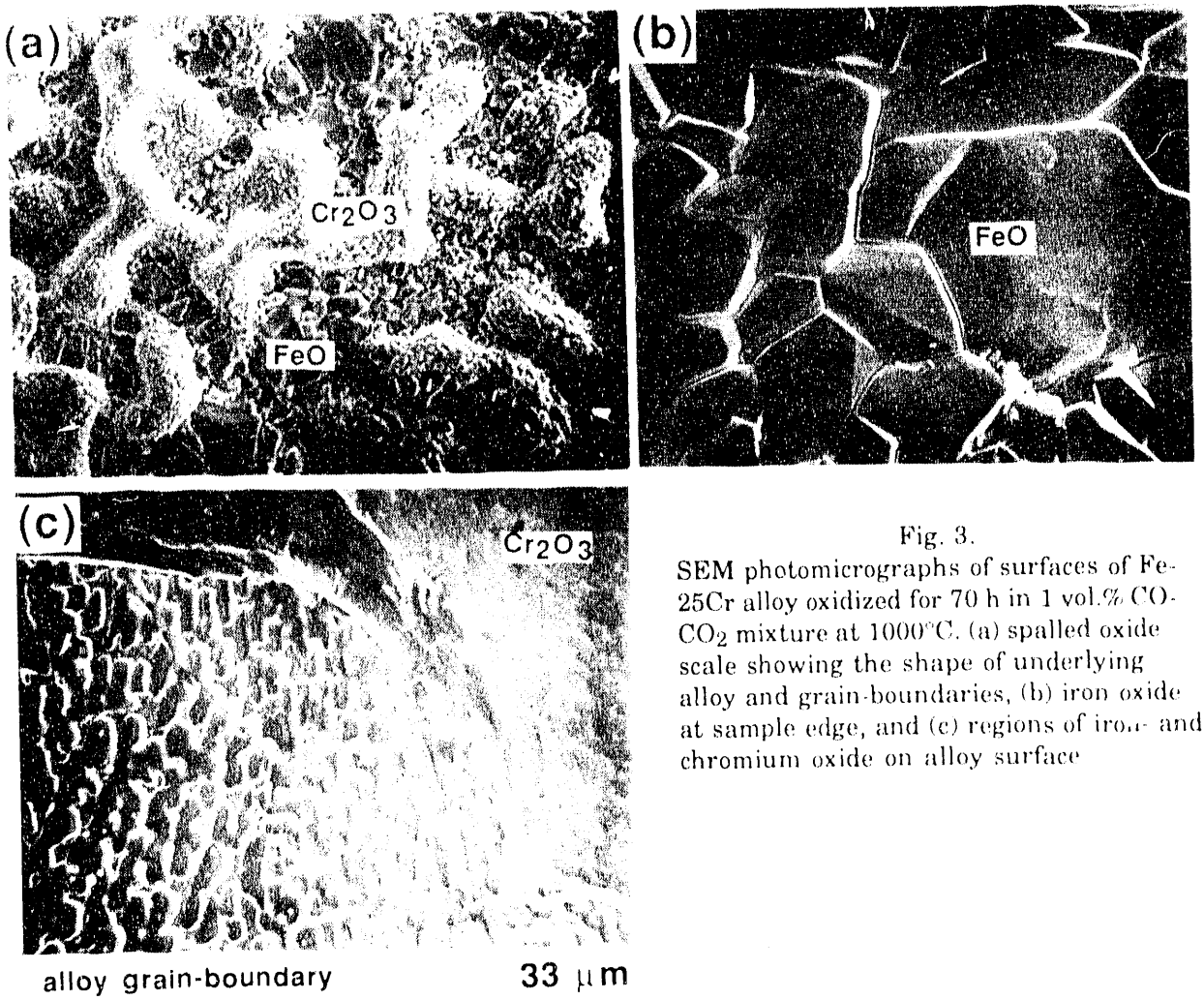

Fig. 3.
SEM photomicrographs of surfaces of Fe-25Cr alloy oxidized for 70 h in 1 vol.% CO-CO_2 mixture at 1000°C. (a) spalled oxide scale showing the shape of underlying alloy and grain-boundaries, (b) iron oxide at sample edge, and (c) regions of iron- and chromium oxide on alloy surface

oxidized at 800 and 700°C, respectively, in several environments. Generally, no oxide spallation was observed in any of the exposed specimens. Whiskers were observed in the specimen tested at 700°C in the 18 vol.% CO-CO_2 gas mixture. A number of investigators have discussed possible mechanisms for the formation of whiskers during oxidation at high temperatures.[14-16] Figure 7 shows SEM photomicrographs of typical oxide/alloy interfaces in specimens oxidized at several temperatures and in different environments. At 1000°C, scale/alloy adhesion is poor, as evidenced by macrovoids at the interface. Table 2 lists parabolic rate constants calculated from (a) TGA and (b) measurements of oxide thicknesses by SEM.

Fe-25Cr-0.3Y

Figure 8 shows SEM photomicrographs of Fe-25Cr-0.3Y alloy oxidized at 1000°C in 1 and 18 vol.% CO-CO_2 gas mixtures. The scale is convoluted and irregular, especially in the specimen exposed to 1 vol.% CO-CO_2 gas mixture. However, the oxide scales were fairly adherent and no cracking or spallation was noted even after thermal quenching of either of the oxidized specimens. Figures 9-11 show SEM photomicrographs of alloy surfaces after oxidation at 900, 800, and 700°C, respectively, in several environments. The oxide grain size was the smallest in the specimen exposed to the lowest-pO_2 atmosphere (i.e., the 18 vol.% CO-CO_2 gas) at all temperatures of the present study. In general, the Y-containing alloy developed adherent oxide scales, in contrast

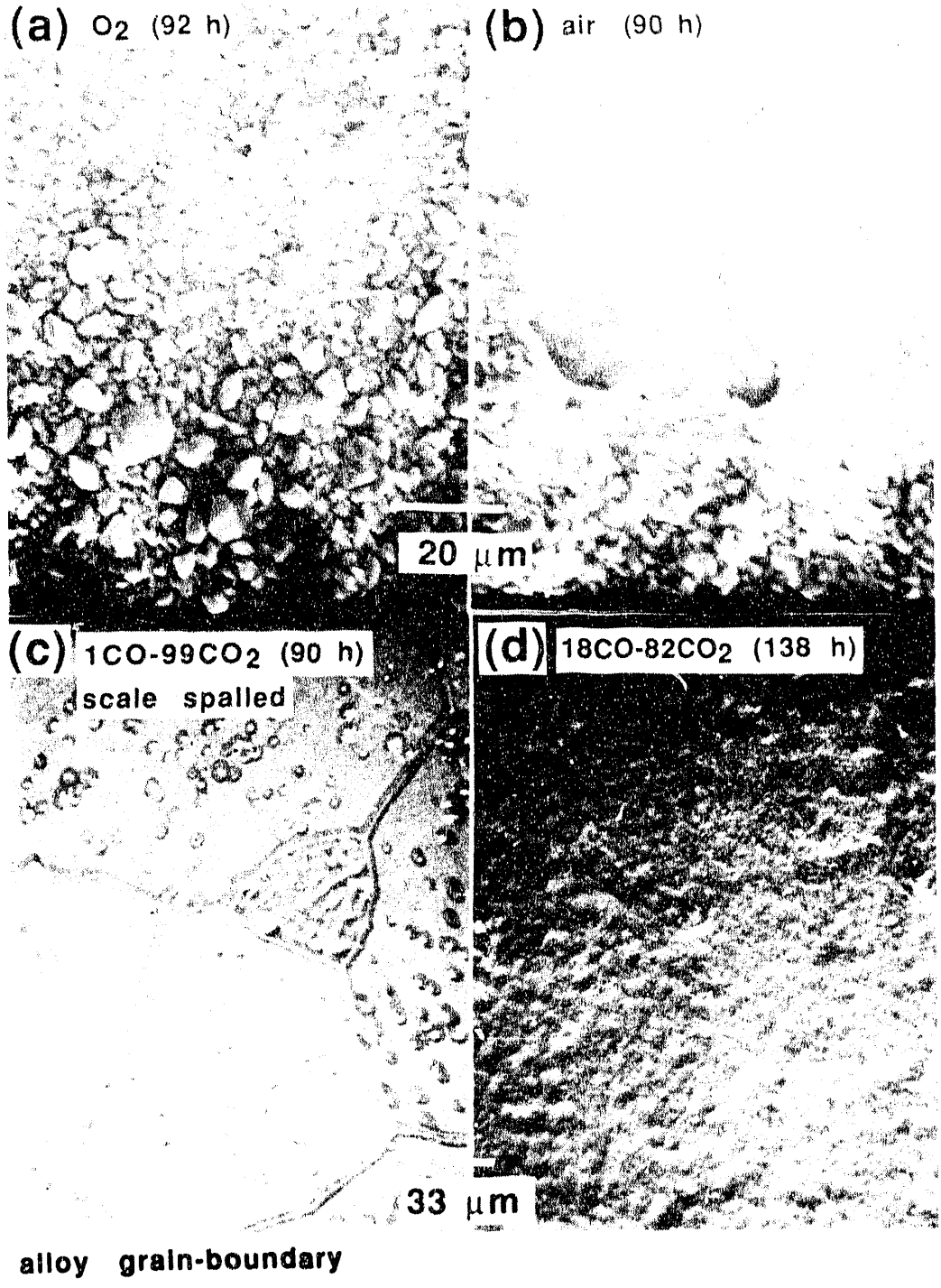

Fig. 4. SEM photomicrographs of Fe-25Cr alloy specimens oxidized at 900°C in several environments: (a) FC-1, (b) FC-22, (c) FC-8, and (d) FC-21

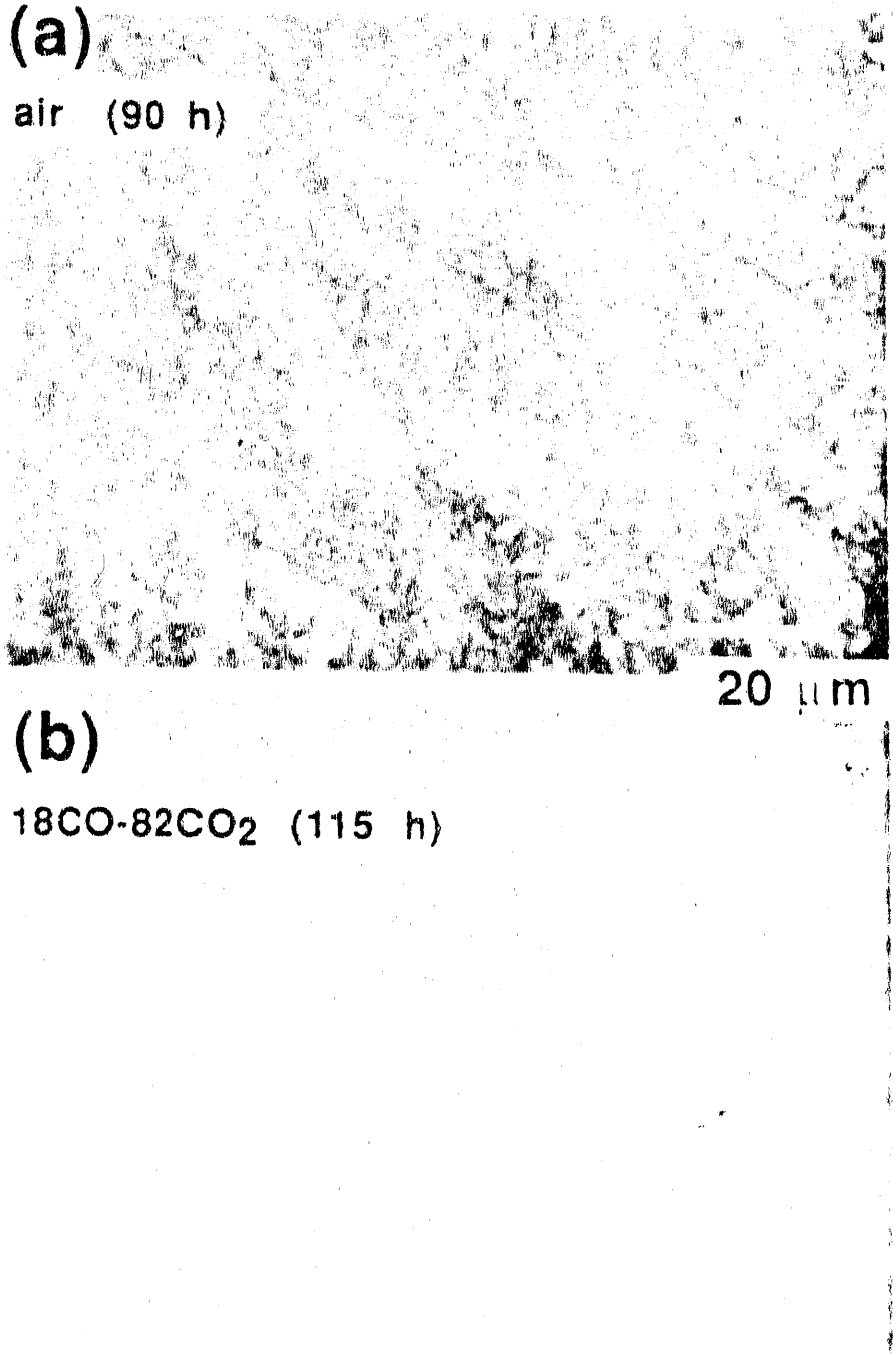

Fig. 5. SEM photomicrographs of Fe-25Cr alloy specimens oxidized at 800°C in several environments: (a) FC-16 and (b) FC-10

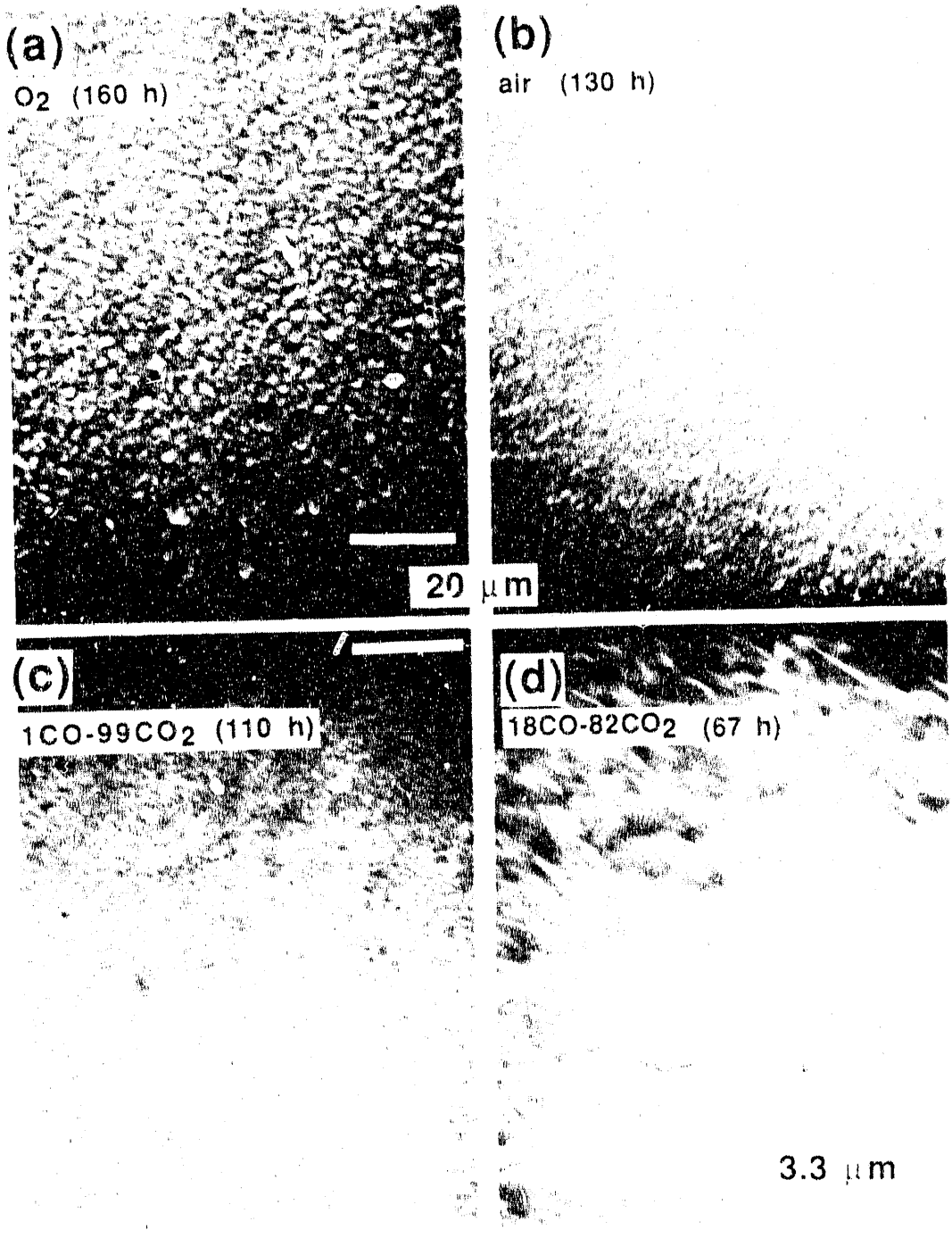

Fig. 6. SEM photomicrographs of Fe-25Cr alloy specimens oxidized at 700°C in several environments: (a) FC-51, (b) FC-3, (c) FC-12, and (d) FC-17

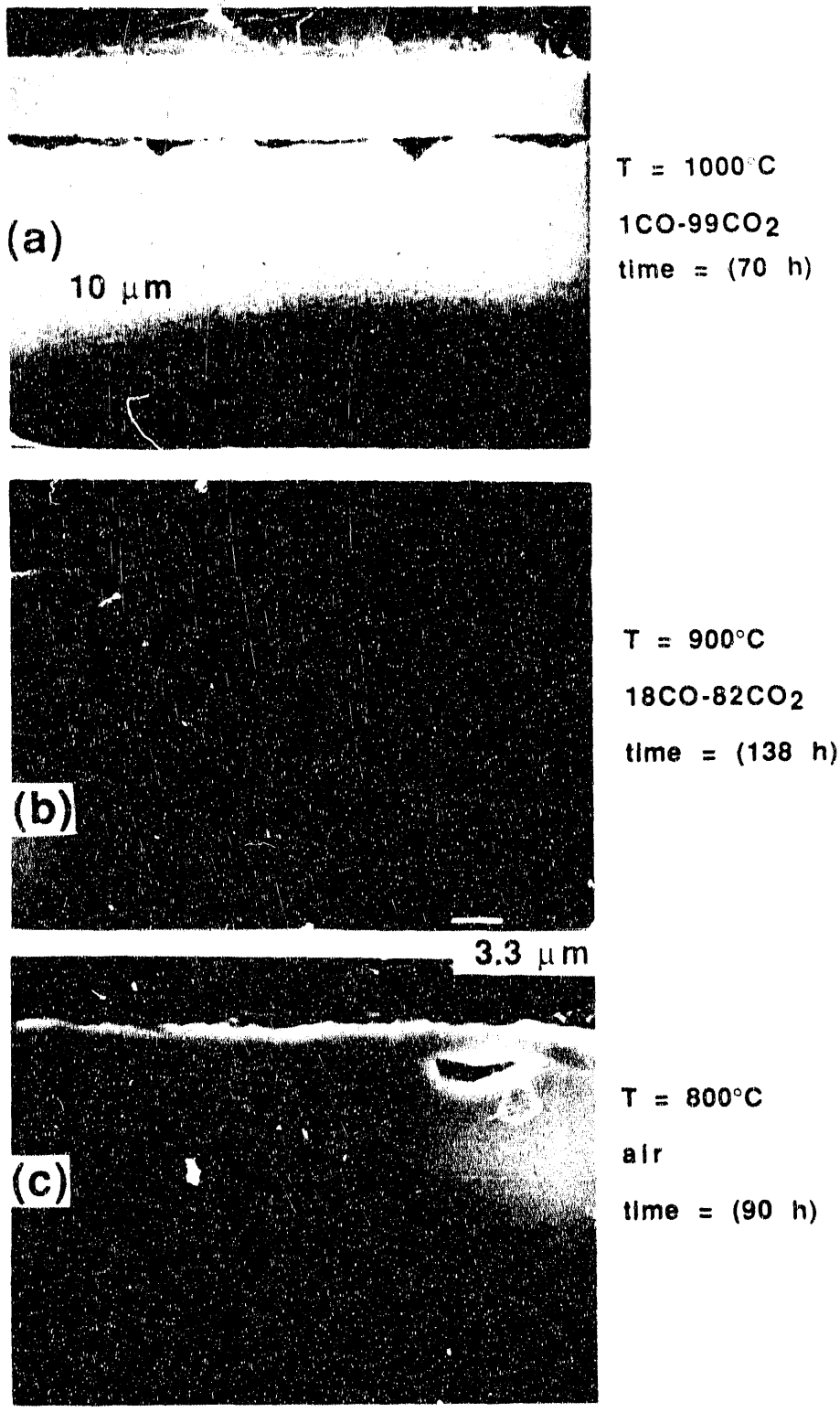

Fig. 7. SEM photomicrographs of cross sections of several oxidized Fe-25Cr specimens: (a) FC-4, (b) FC-21, and (c) FC-16

Table 2. Parabolic rate constants derived from TGA data and scale thickness measurements (cm^2/s) for Fe-25Cr alloy[a]

Environment and Rate Constant	1000°C	900°C	800°C	700°C
Oxygen	FC-2 (94)	FC-1 (92)	FC-11 (135)	FC-51 (160)
Kp(TGA)	7.6×10^{-12}	2.2×10^{-13}	2.0×10^{-13}	1.0×10^{-15}
Kp(SEM)	–	2.3×10^{-12}	–	6.3×10^{-15}
Air	FC-5 (40)	FC-22 (90)	FC-16 (90)	FC-3 (130)
Kp(TGA)	1.2×10^{-11}	7.1×10^{-13}	2.3×10^{-13}	9.5×10^{-15}
Kp(SEM)	–	–	5.2×10^{-13}	1.4×10^{-14}
1%CO-CO_2	FC-4 (70)	FC-8 (90)	FC-14 (140)	FC-12 (110)
Kp(TGA)	5.1×10^{-10}	3.1×10^{-12}	3.5×10^{-13}	4.9×10^{-14}
Kp(SEM)	1.1×10^{-11}	5.8×10^{-13}	–	5.6×10^{-14}
18%CO-CO_2	FC-88 (120)	FC-2 (138)	FC-10 (115)	FC-17 (67)
Kp(TGA)	6.5×10^{-12}	1.4×10^{-12}	2.0×10^{-13}	1.4×10^{-13}
Kp(SEM)	–	1.5×10^{-12}	1.3×10^{-13}	9.3×10^{-14}

[a]FC-# indicate Fe-25Cr alloy, and numbers in parentheses indicate exposure times in hours; K_p(TGA) and K_p(SEM) are in cm^2/s.

with those developed on the Y-free alloy, which exhibited a propensity to spall on thermal quenching. Figure 12 shows SEM photomicrographs of typical oxide-alloy interfaces in Fe-25Cr-0.3Y specimens oxidized at several temperatures and in different environments. Occasionally, a void of the type shown in Fig. 12(b) is observed at the alloy/scale interface of the oxidized specimen. Yttrium oxide was found in the void region, and a similar observation had been made earlier.[17] The presence of yttrium oxide at the scale/metal interface can result in local blocking of cations from the alloy to the external scale. Further, cation mixing in chromium oxide-yttrium oxide can lead to formation of $YCrO_3$ with a pervoskite structure.[18-21] At temperatures below 800°C, no significant difference in the oxidation rate and in scale morphologies was noted between the alloys with and without Y. Table 3 lists the parabolic rate constants derived from an analysis of TGA data and determined from oxide thickness measurements by SEM.

The parabolic rate constants (Kp) obtained from TGA and SEM data for Fe-25Cr alloy are plotted in Figs. 13 and 14, at high and low pO_2, respectively. At high pO_2, the Kp values determined from SEM measurements were somewhat higher than those calculated from TGA data, probably because of increased porosity of the scales developed in high-pO2 environments. At low pO_2s, the rate constants determined by both approaches agree fairly well except for one specimen exposed at 1000°C in 1 vol.% CO-CO_2 gas. In this specimen (FC-4), a copious amount of iron oxide formed on the edges of the specimen (as shown in Fig. 3). Figures 15 and 16 show Kp values (obtained by TGA and SEM) for Fe-25Cr-0.3Y alloy in high- and low-pO_2 environments. In general, the values obtained from TGA data were higher than those determined by SEM. This trend could be explained by the presence of Y in the alloy as yttrium oxide particles because yttrium oxide is thermodynamically more stable than both chromium oxide and iron oxide.[22] This would contribute to weight gain but not to scale thickness. The presence of Y also slows the transport of cations such as Cr and Fe, as evidenced by the absence of iron oxide in the scales

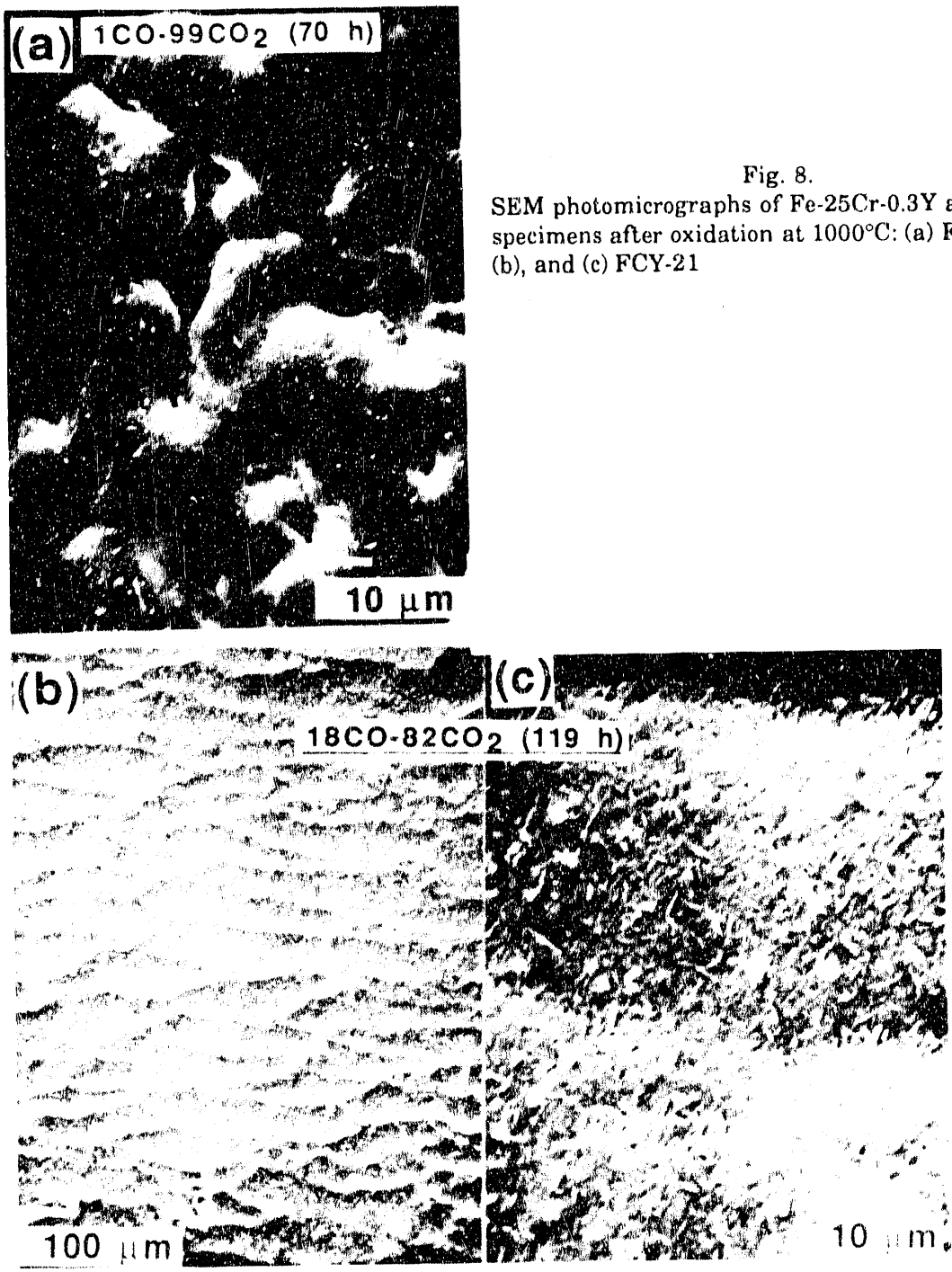

Fig. 8.
SEM photomicrographs of Fe-25Cr-0.3Y alloy specimens after oxidation at 1000°C: (a) FCY-22, (b), and (c) FCY-21

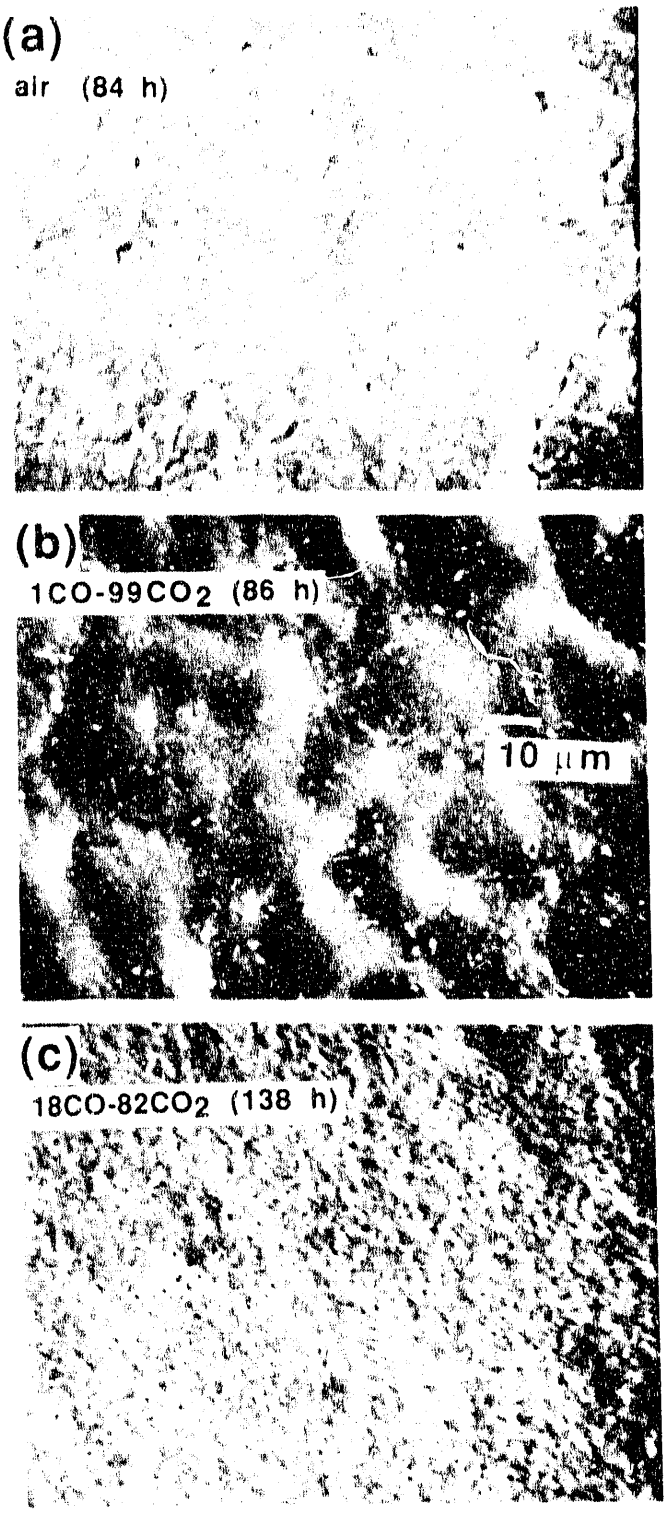

Fig. 9. SEM photomicrographs of Fe-25Cr-0.3Y alloy specimens oxidized at 900°C in several environments: (a) FCY-26, (b) FCY-6, (c) FCY-77

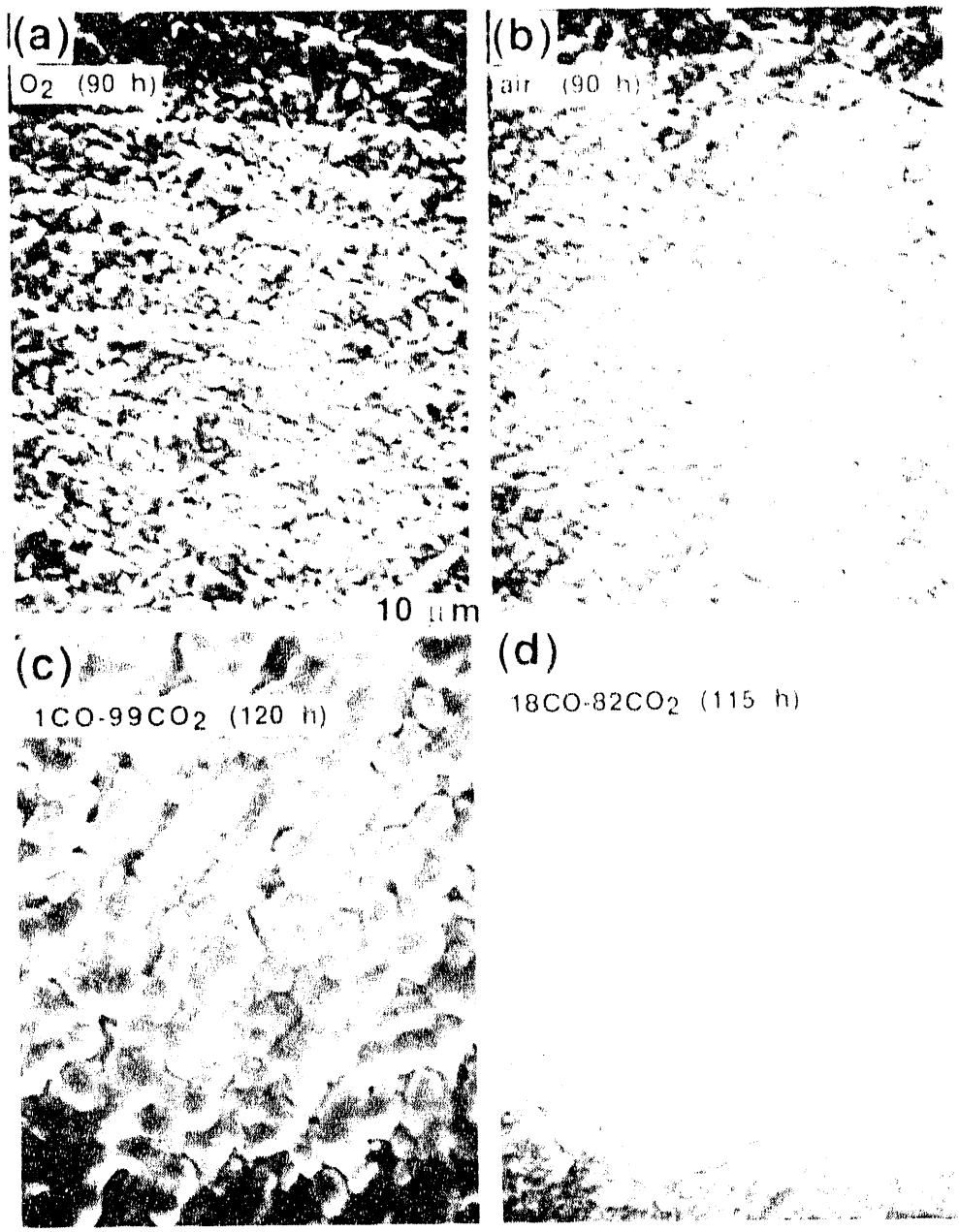

Fig. 10. SEM photomicrographs of Fe-25Cr-0.3Y alloy specimens oxidized at 800°C in several environments: (a) FCY-0, (b) FCY-2, (c) FCY-4, and (d) FCY-24

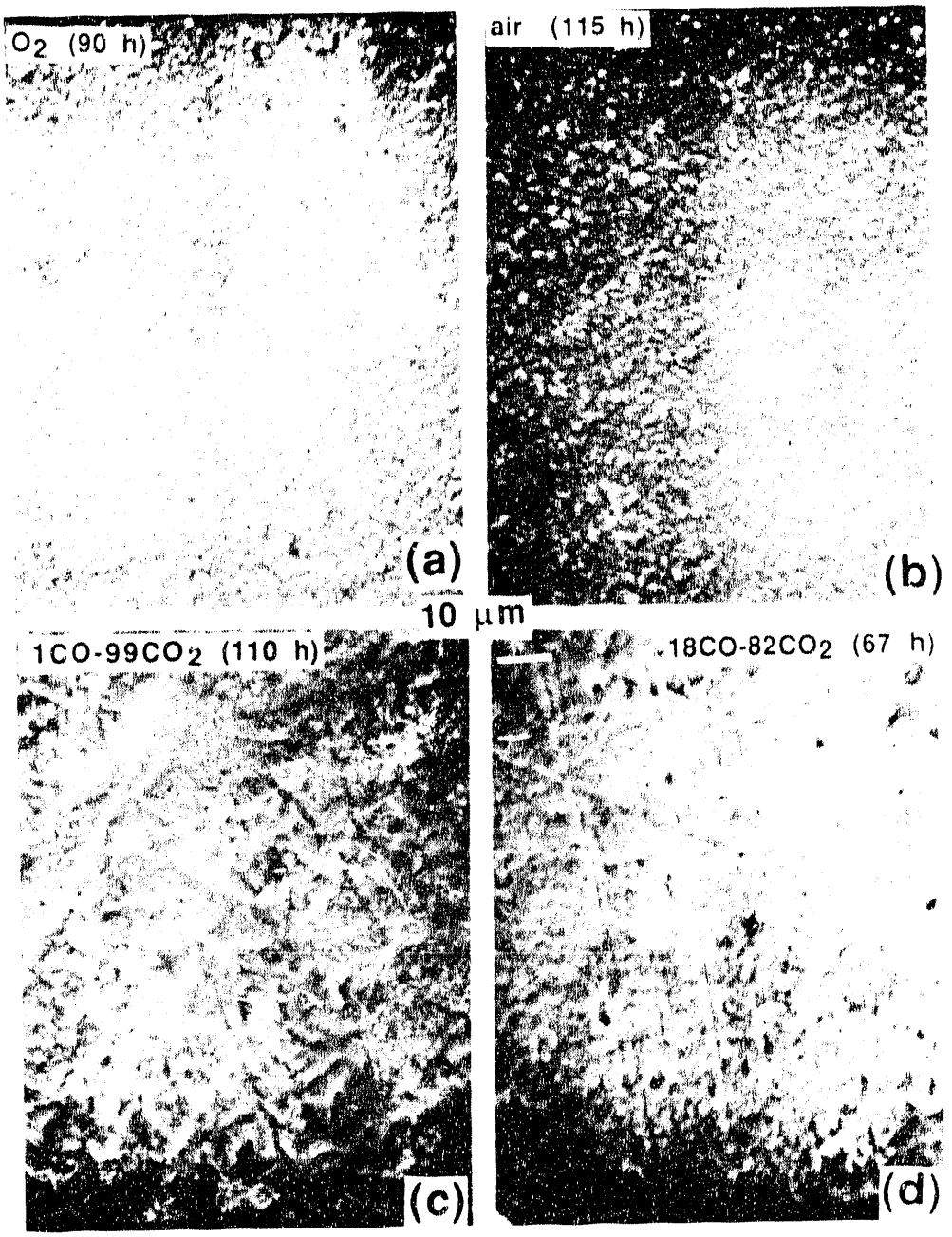

Fig. 11. SEM photomicrographs of Fe-25Cr-0.3Y alloy specimens oxidized at 700°C in several environments: (a) FCY-1, (b)FCY-11, (c) FCY-33, and (d) FCY-66

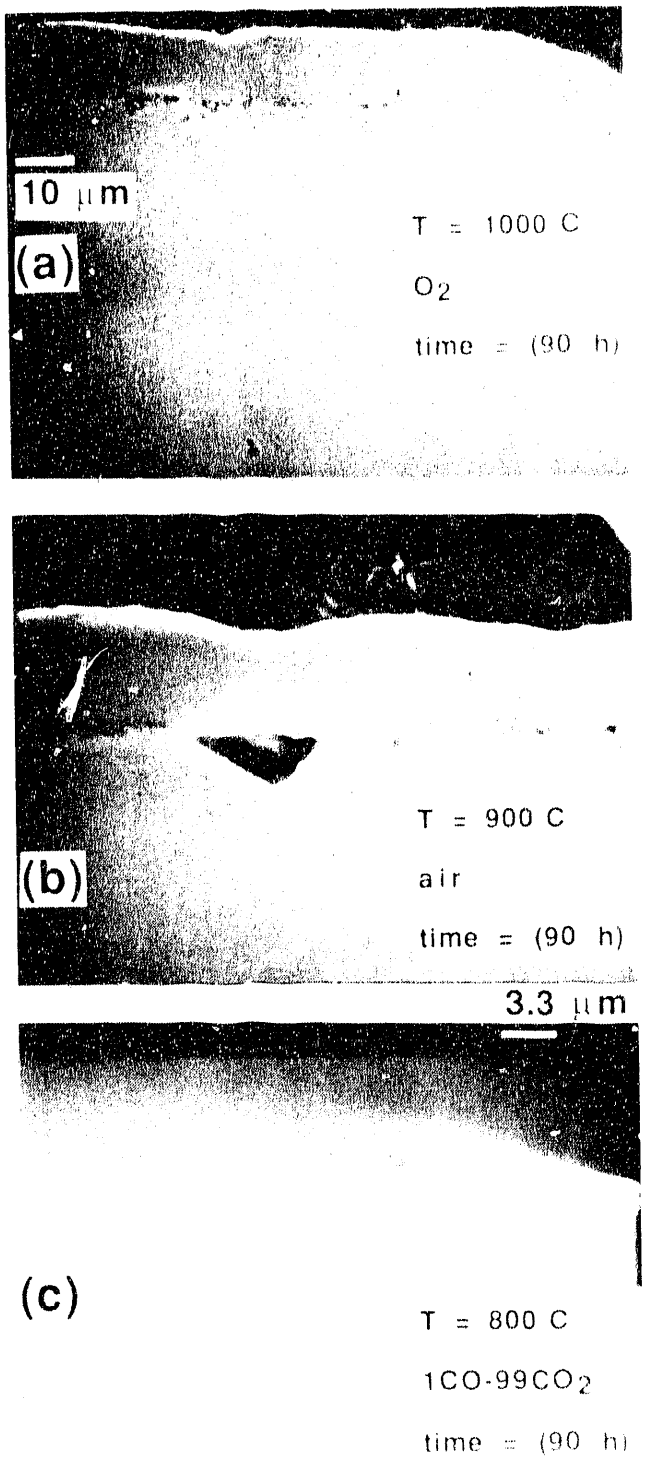

Fig. 12. SEM photomicrographs of cross sections of several oxidized Fe-25Cr-0.3Y specimens: (a) FCY-22, (b) FCY-6, and (c) FCY-0

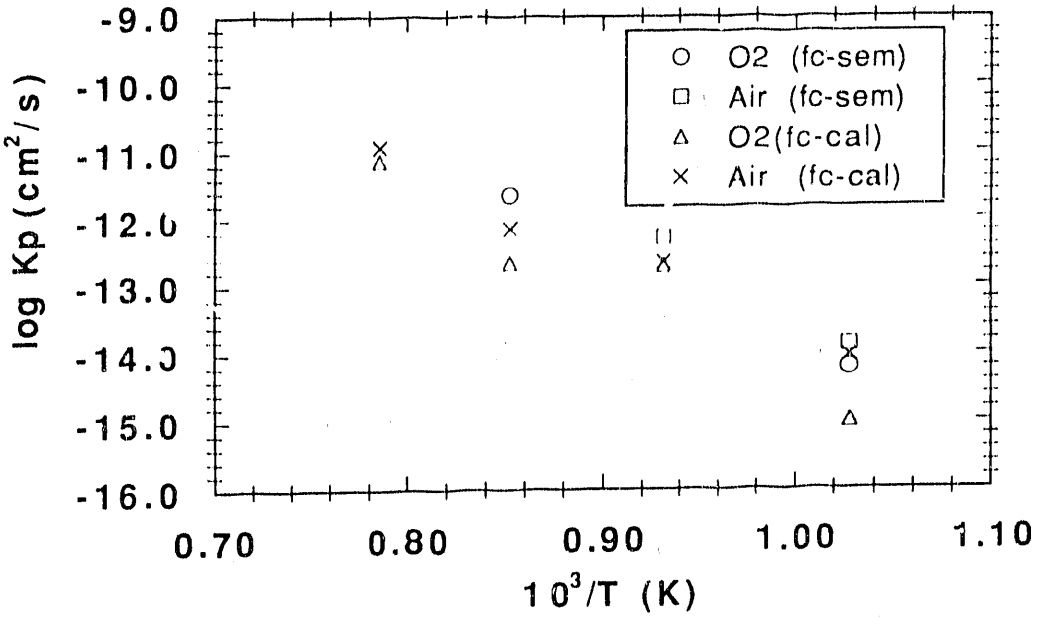

Fig. 13. Temperature dependence of parabolic rate constant for oxidation of Fe-25Cr alloy in a high-pO_2 environment

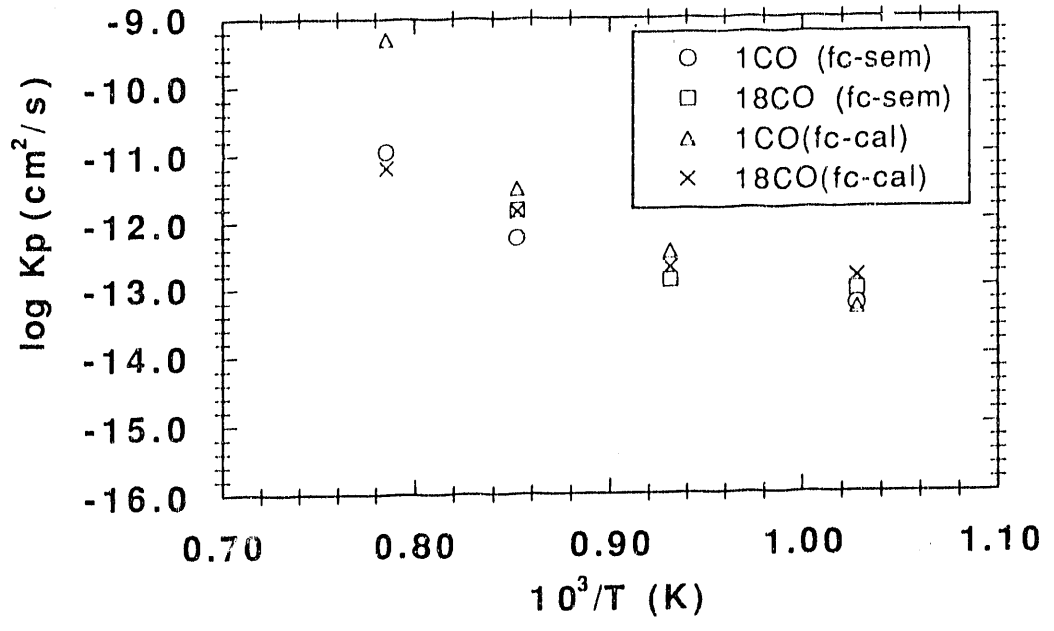

Fig. 14. Temperature dependence of parabolic rate constant for oxidation of Fe-25Cr alloy in a low-pO_2 environment

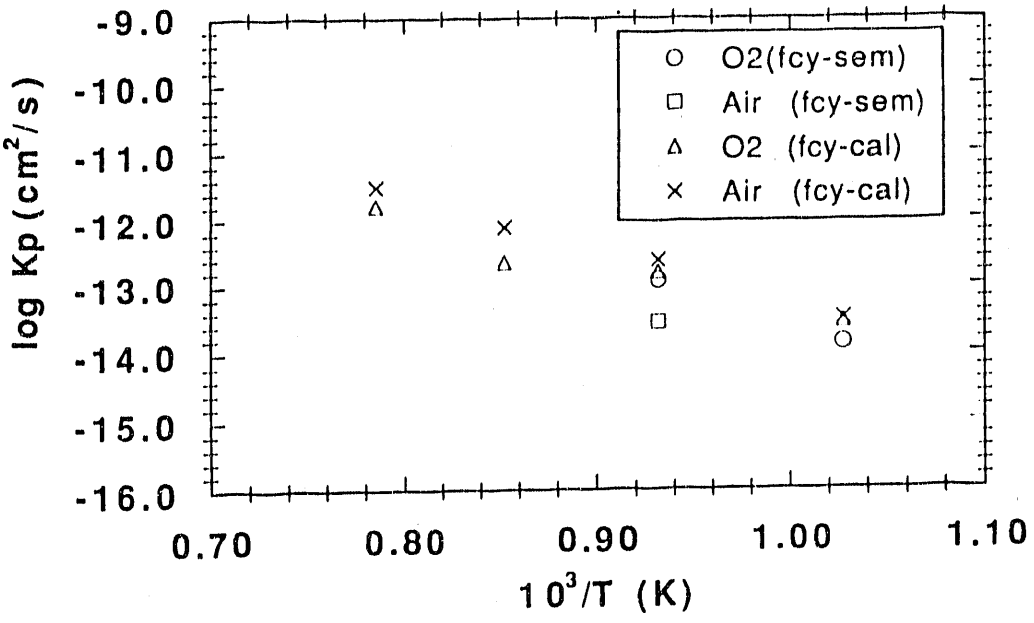

Fig. 15. Temperature dependence of parabolic rate constant for oxidation of Fe-25Cr-0.3Y alloy in a high-pO_2 environment

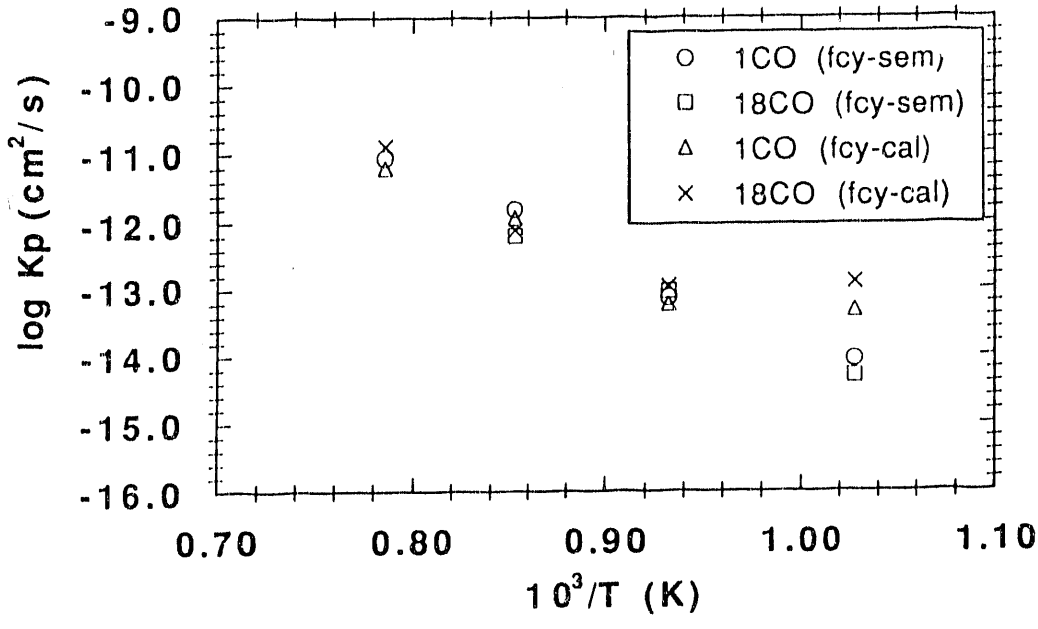

Fig. 16. Temperature dependence of parabolic rate constant for oxidation of Fe-25Cr-0.3Y alloy in a low-pO_2 environment

Table 3. Parabolic rate constants derived from TGA data and scale thickness measurements (cm^2/s) for Fe-25Cr-0.3Y alloy[a]

Environment and Rate Constant	1000°C	900°C	800°C	700°C
Oxygen	FC-3 (120)	FC-7 (98)	FC-0 (90)	FC-1 (90)
Kp(TGA)	1.7×10^{-12}	2.3×10^{-13}	1.6×10^{-13}	2.9×10^{-14}
Kp(SEM)	–	–	1.2×10^{-13}	1.4×10^{-14}
Air	FC-8 (74)	FC-26 (84)	FC-2 (90)	FC-11 (115)
Kp(TGA)	3.2×10^{-12}	7.8×10^{-13}	2.4×10^{-13}	1.3×10^{-45}
Kp(SEM)	–	–	2.9×10^{-14}	–
1%CO-CO_2	FC-22 (70)	FC-6 (86)	FC-4 (120)	FC-33 (110)
Kp(TGA)	6.3×10^{-12}	1.2×10^{-12}	6.2×10^{-14}	4.9×10^{-14}
Kp(SEM)	8.9×10^{-12}	1.6×10^{-12}	7.8×10^{-14}	9.1×10^{-15}
18%CO-CO_2	FC-21 (119)	FC-77 (138)	FC-24 (115)	FC-66 (67)
Kp(TGA)	1.3×10^{-11}	7.8×10^{-13}	1.1×10^{-13}	1.4×10^{-13}
Kp(SEM)	–	6.5×10^{-13}	9.5×10^{-14}	5.1×10^{-15}

[a]FCY-# indicate Fe-25Cr-0.3Y alloy, and numbers in parentheses indicate exposure times in hours; K_p(TGA) and K_p(SEM) are in cm^2/s.

developed in Y-containing alloys exposed to the wide range of oxidizing environments and temperatures used in this study. At 700°C and in low-pO_2 environments (see Fig. 16), Kp values obtained by TGA are substantially higher than those measured by SEM analysis, indicating the dominance of internal oxidation as the mode of oxidation at lower temperatures.

Oxidation of Fe-25Cr, Fe-25Cr-1Ce, and Fe-25Cr-1Y Alloys at 1000°C

Figure 17 shows a cross–sectional view of scales spalled from Fe-25Cr alloy oxidized for 24 h and quenched to room temperature. The spalled scales were convoluted and totally separated from the substrate without any transverse cracks. Figure 18 shows details of different regions of the scale illustrated in Fig. 17. Most edge cracks in the 15-20 μm scale were 1-2 μm from the scale/alloy interface. Such cracks are caused by a release of stored energy along the scale plane direction near the scale/alloy interface region.[23] Figure 19 shows the fracture surface of the spalled scale, which was predominantly high-density chromia, based on SEM and energy-dispersive X-ray (EDX) analysis. The composition of both sides of the spalled scale was pure chromium oxide, as can be seen from the EDX spectra shown in Fig. 20. Figure 21 shows different areas of the alloy surface after the removal of spalled scale. These photomicrographs show tiny particles of chromium oxide (based on an EDX analysis) on the alloy surface. The presence of these particles on the alloy side of the scale/alloy interface indicates that (a) Cr vaporization and its subsequent oxidation occurred at the reduced pO_2 level prevalent at the interface, (b) separation of scale from alloy occurred at an earlier stage before spallation, and (c) the separation gap between the alloy and scale should be wider than the average dimension (1 μm) of particles at the interface. Further, the presence of very fine grooves on the alloy surface (see Fig. 21) may be evidence for good adhesion between scale and alloy in the early stage of oxidation.

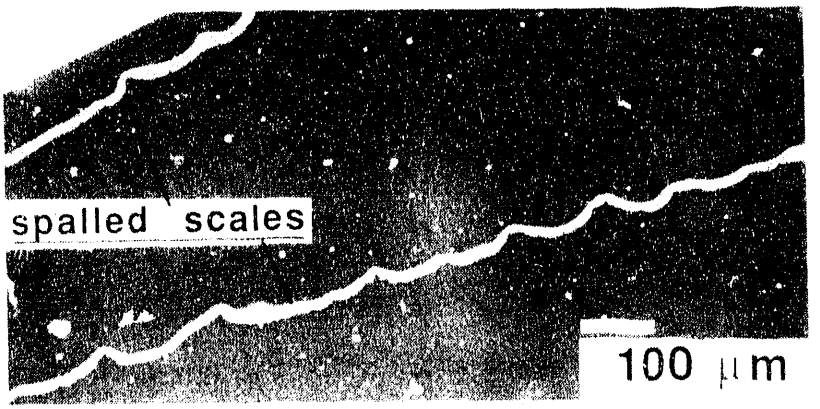

Fig. 17. Cross–sectional view of totally spalled scale from an Fe-25Cr alloy specimen after 24–h oxidation

Figure 22 shows SEM photomicrographs of surfaces of a sample that was reoxidized after the original oxide had spalled. There was no spallation of oxide scale even though the reoxidized sample was thermally quenched in a manner similar to that for the original oxide. For short–time oxidation (50 h or less at 1000°C), the oxide scale was pure chromium oxide and no Fe was detected either in the grain boundaries or in the interior of the grains. Over longer periods of oxidation, the sample showed abrupt increase in weight, as shown in Fig. 23 for Fe-25Cr alloy oxidized at 1000°C in a high-pO_2 atmosphere. Detailed SEM and EDX analysis of the specimen showed copious growth of iron oxide on the scale surface, as seen in Figs. 24-26. The smooth and rough areas in Fig. 25 are chromium oxide and iron oxide, respectively. Analysis also showed enhanced transport along grain boundaries, as evidenced by the relief of these boundaries in the SEM photomicrographs. Details are presented in Fig. 26 on the formation of iron oxide on the gas side of the scale. The aggressiv. extrusion of iron oxide shows that Fe transports through preferred channels (e.g., grain boundaries, open pores) and subsequently oxidizes on the gas side of the interface. Figure 27 shows pyramid–shaped iron oxide; the open pyramid tops indicate that oxide growth is probably controlled by surface diffusion. Further, the oxide protrusions are spaced at regular intervals of ≈0.2 μm. Figure 28 shows the oxidation process in cross section, together with details of the oxide morphologies and thicknesses of different layers. Table 4 lists the chemical compositions of different scale layers observed during oxidation of an Fe-25Cr alloy.

Figure 29 shows weight change data as a function of exposure time for oxidation of Fe-25Cr and Fe-25Cr-0.3Y alloys at 1000°C in low-pO_2 environments. The data clearly show that the formation of iron oxide in the scale, which was observed during oxidation of Fe-25Cr alloy in 1 vol.% CO-CO_2 gas mixture, leads to a substantial increase in oxidation rate. Yttrium–containing alloys developed only chromium oxide scales and exhibited low rates of oxidation. Figures 30-32 show cross sections of Fe-25Cr, Fe-25Cr-1Ce, and Fe-25Cr-1Y alloy samples, respectively, after oxidation for 24 hr at 1000°C. Whereas the scale on the Fe-25Cr alloy was prone to spallation, the scales developed on Ce- and Y-containing alloys were adherent to the substrate alloy. In the Ce-containing alloy, iron oxide did not form even after oxidation for 120 hr. Some segregation of Ce to the grain boundaries in the scale and in the substrate alloy was observed. According to the phase diagram, Ce forms no compound with Cr, but only with Fe (4.5Fe-95.5Ce, which melts at 640°C).[24]

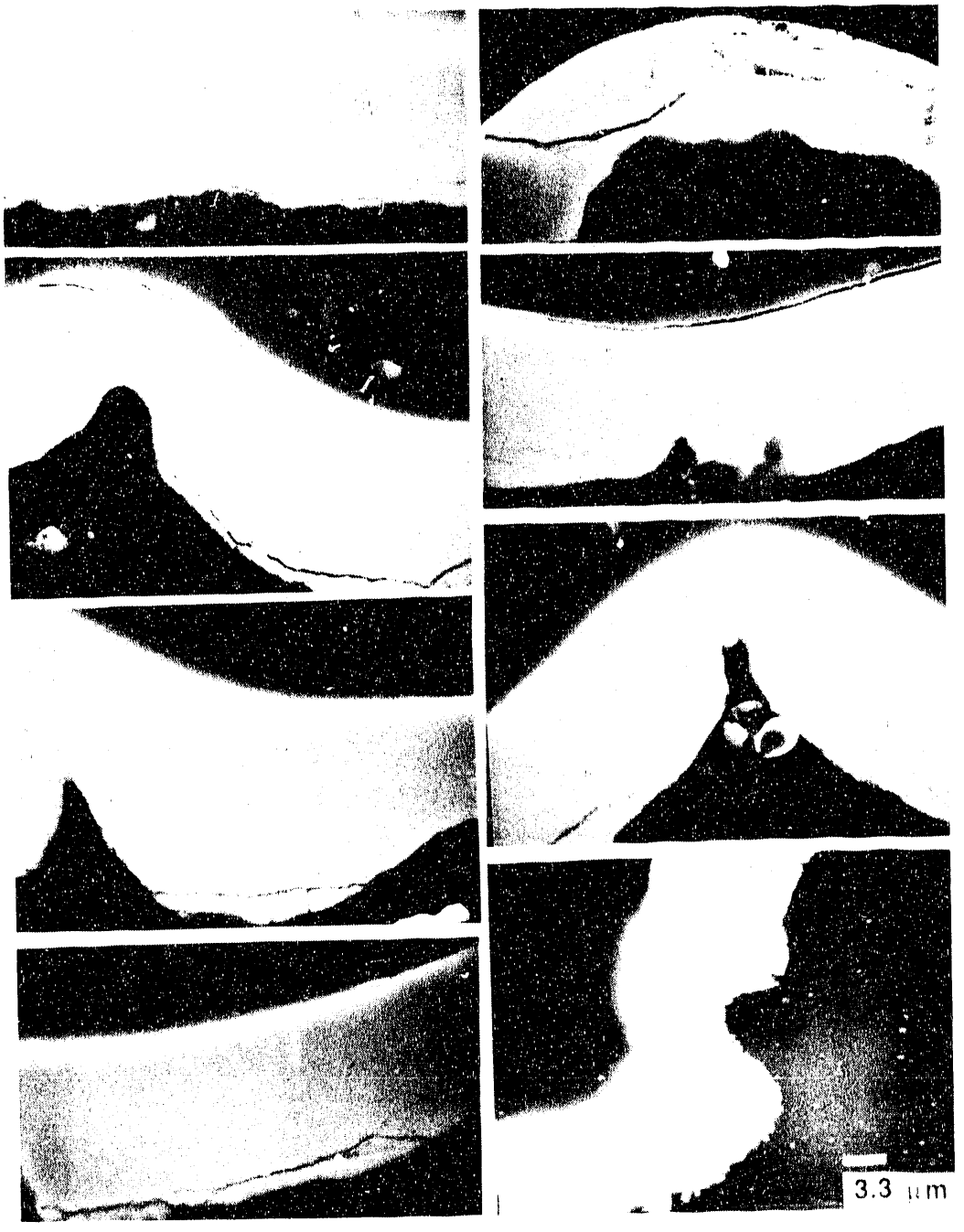

Fig. 18. SEM photomicrographs of different regions of Fig. 17

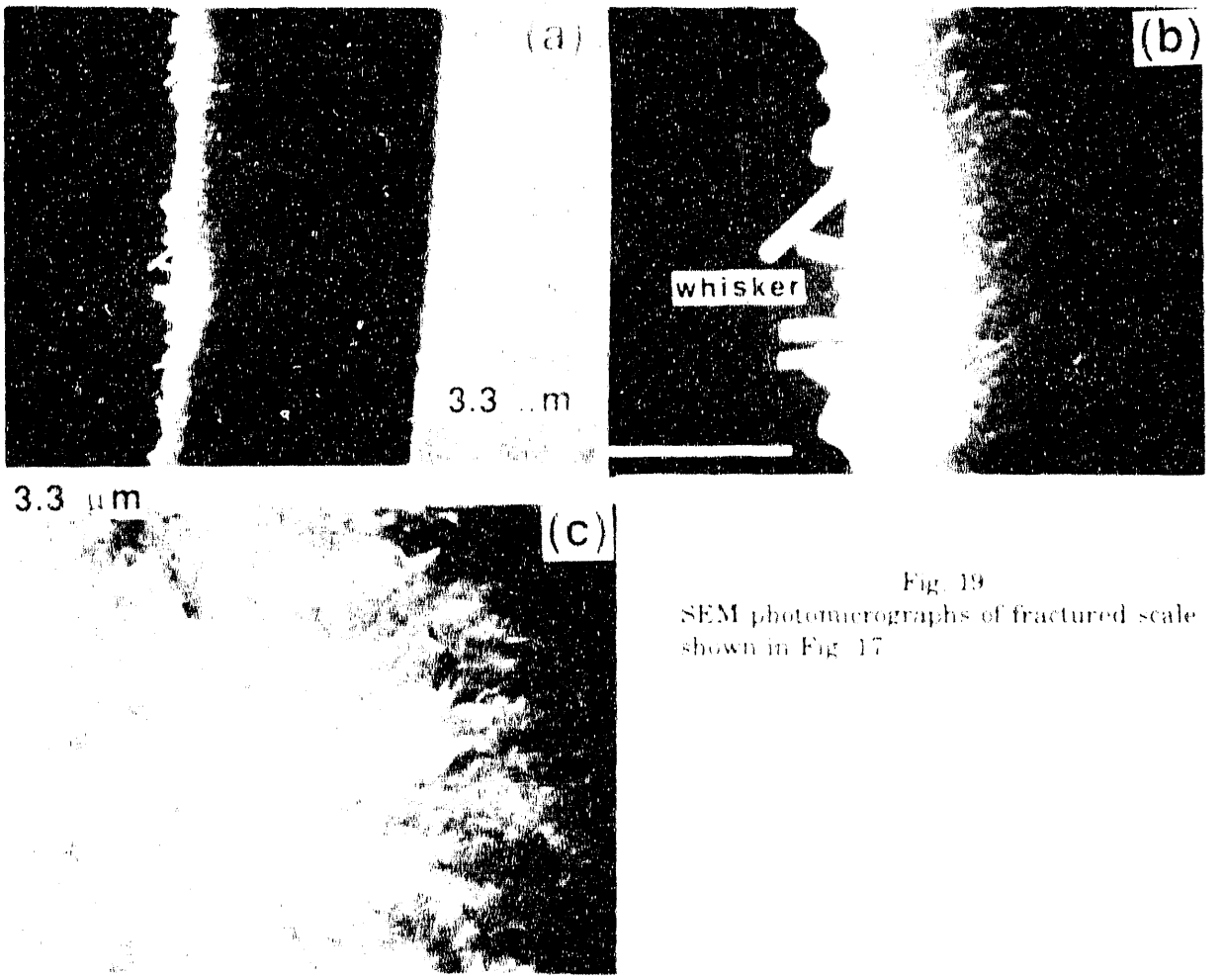

Fig. 19
SEM photomicrographs of fractured scale shown in Fig. 17

Based on the literature, the solid solubility of Y in Cr is 0.71 at.% and that for Cr in Y is 0.70 at.%. However, on the basis of the difference in the respective atomic radii of Cr and Y, the solid solubility of Y in Cr is reported to be <0.005 at.%.[25] The compound Y_2Fe_{17} with a hexagonal crystal structure has been identified in the Fe-Y phase diagram. In previous studies on Fe-25Cr-0.87Y alloy, a compound of composition $Y_2Fe_2Cr_{15}$ has been observed in the grain-boundary regions of the alloy.[17] Yttrium could be detected by EDX (see Fig. 33) in the grain boundaries in the scale and in the scale/alloy interface regions of the oxidized Fe-25Cr-Y alloy that contained Y at 1.0 wt.% but not at 0.3 wt.%.

Figure 34 shows thermogravimetric data for Fe-25Cr, Fe-25Cr-1Y, and Fe-25Cr-1Ce alloys oxidized at 1000°C. The rate of weight change is similar for the base alloy and that containing Ce. The rate for the Y-containing alloy is somewhat lower. Scale thickness measurements showed no appreciable difference between the Ce- and Y-containing alloys. The difference in weight change between the two alloys is probably due to the increased level of internal oxidation in Ce-containing alloy. One striking difference in the scaling behavior between these alloys is the total spallation in the base alloy and fully adherent scale in the doped alloys. Repeated oxidation of the samples (with the removal of the spalled scale from the Fe-25Cr alloy and of adherent scales from the doped alloys) showed that the scales formed during the second exposure were adherent in all the samples even after thermal quenching. Further, during the first oxidation, a large grain growth

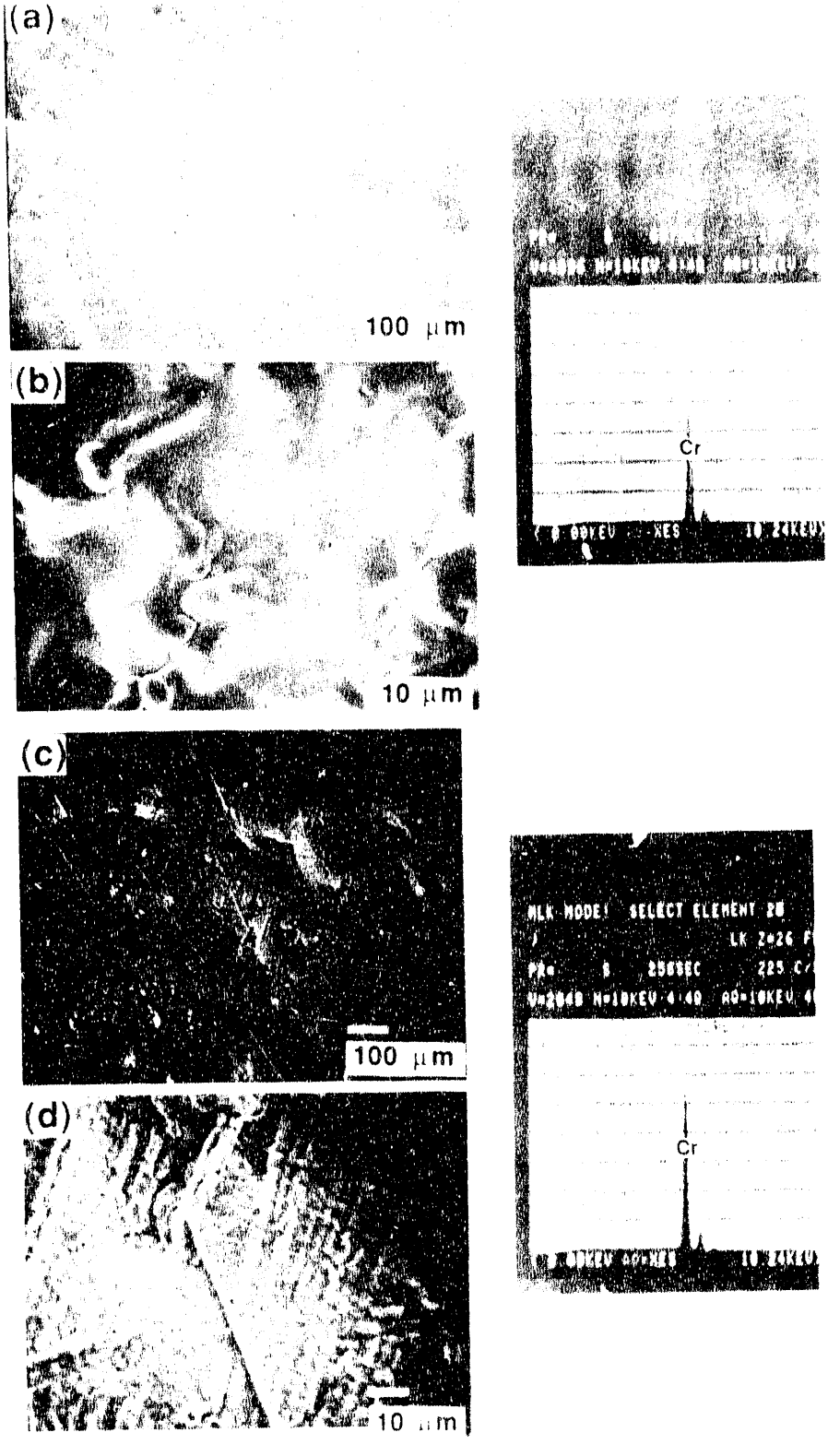

Fig. 20. SEM photomicrographs and EDX analysis of different regions of Fig. 17: (a) scale/gas interface and (c) alloy/scale interface; (b) and (d) represent magnified views of (a) and (c)

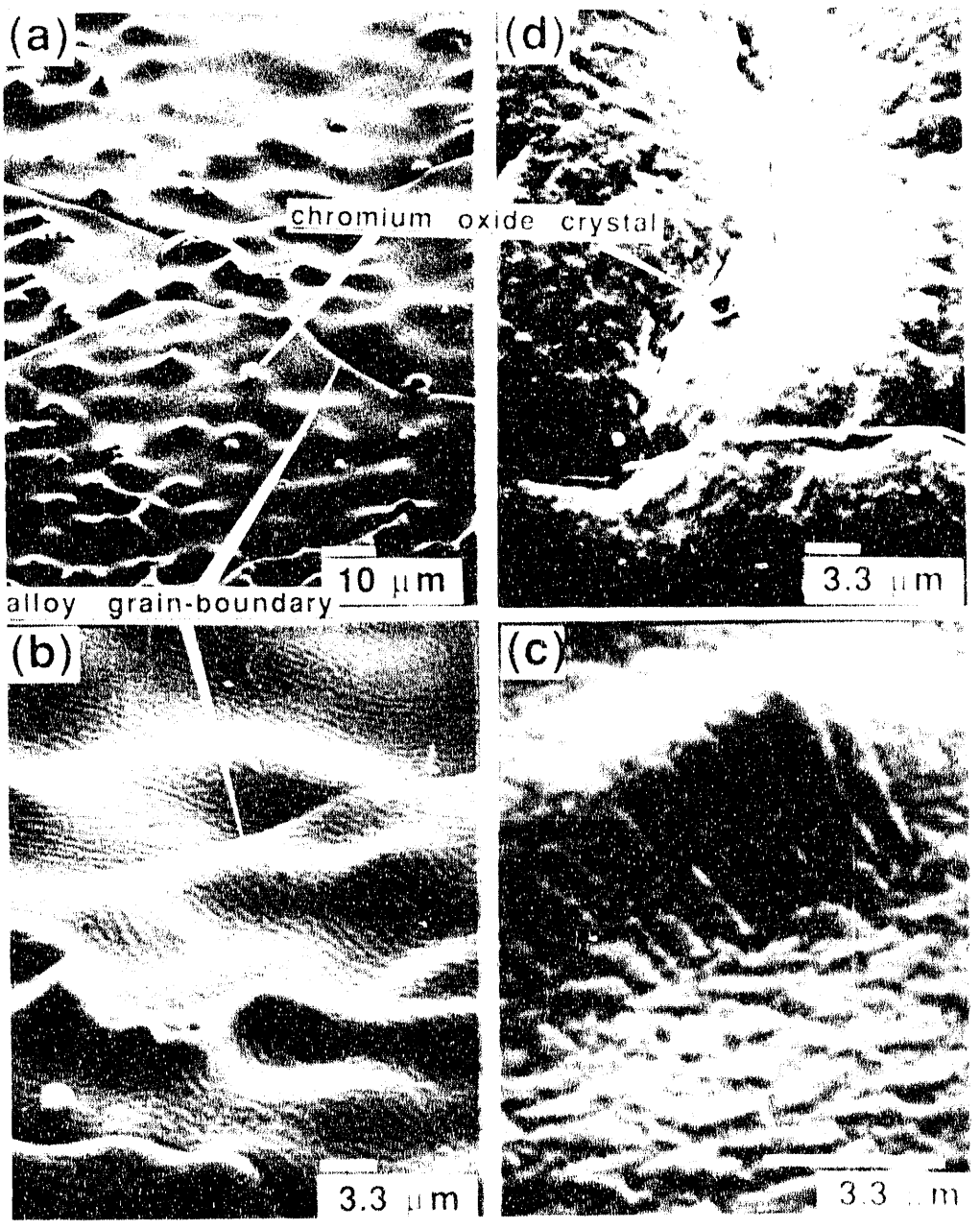

Fig. 21. (a)-(c): Fe-25Cr alloy surface of spalled oxide scale; (d): scale side of alloy/scale interface

occurred in the base alloy and a much smaller growth resulted during the second exposure. The alloy grain growth in the doped-alloys was small during both exposures. Figure 35 shows the cross sections of Fe-25Cr alloy specimens oxidized at temperatures of 700 to 1000°C. Figure 36 shows the cross sections of Y-containing alloys oxidized at different temperatures. Figure 37 shows variation in grain size for an alloy with and without Y as a function of exposure temperature. It is evident that at 700 C, the lowest temperature of this study, reactive–element addition has almost no effect on grain growth. Figure 38 is a plot of grain–size increase as a function of reciprocal temperature for the Fe-25Cr base alloy.

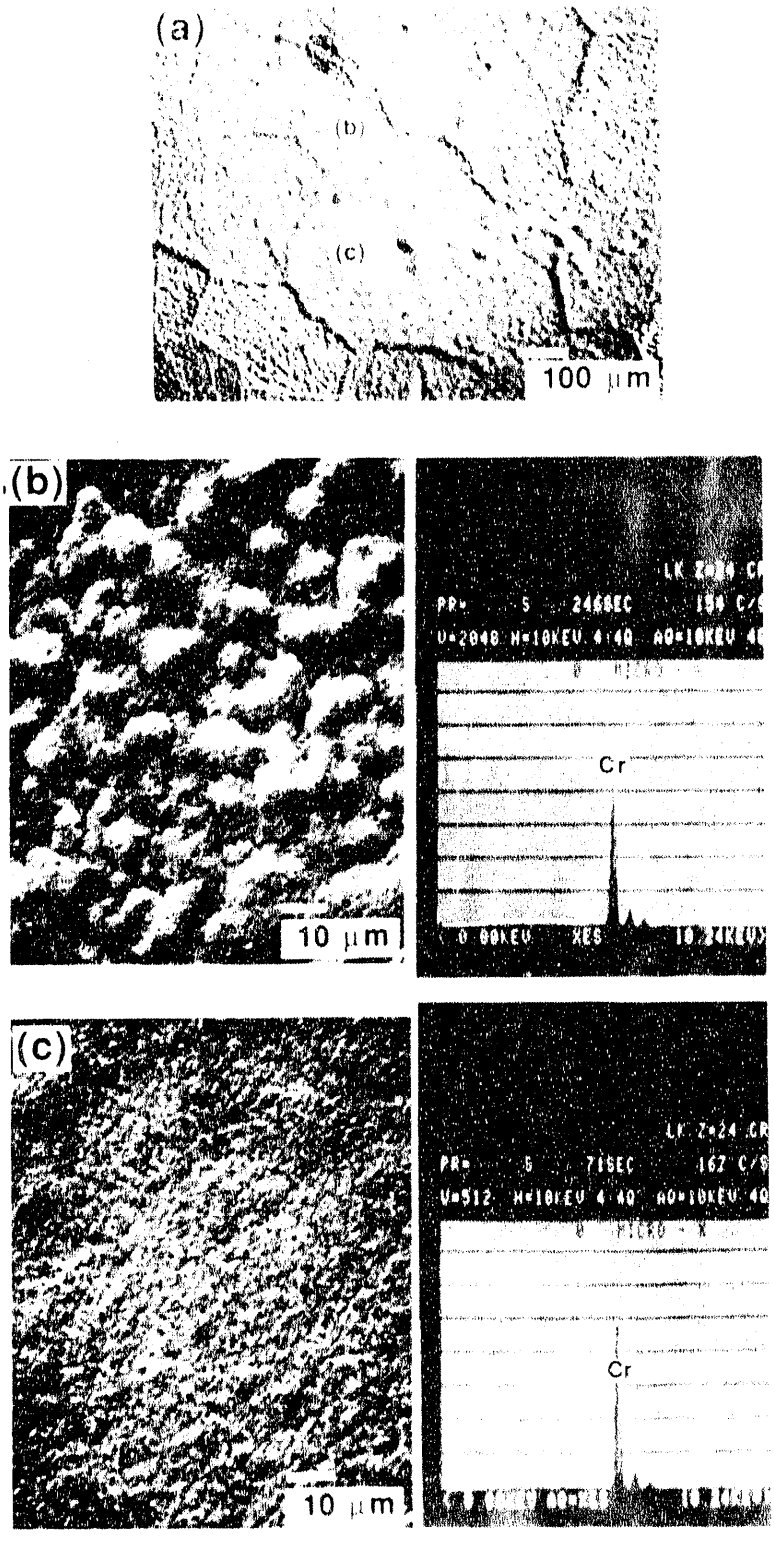

Fig. 22. SEM photomicrographs and EDX analysis of surface of Fe-25Cr alloy reoxidized: (a) overall oxide surface, (b) rough area in (a), and (c) smooth area in (a)

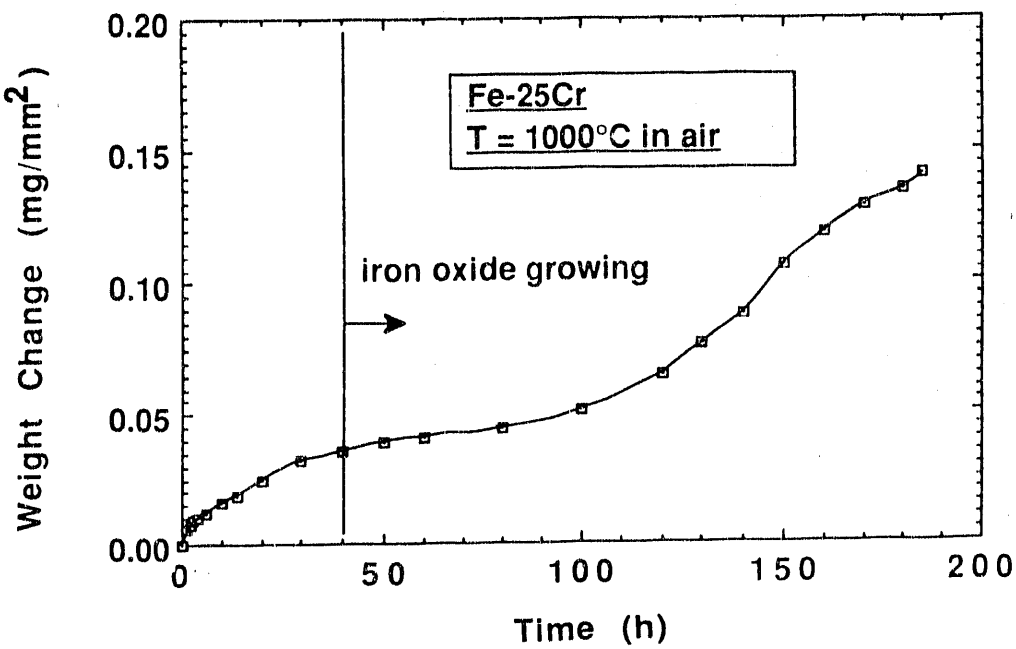

Fig. 23. Weight change versus time for second oxidation of Fe-25Cr alloy at 1000°C

Alloy Grain Growth

To evaluate the role of reactive–element addition in the grain–growth process in the absence of oxidation, samples of Fe-25Cr, Fe-25Cr-1Ce, and Fe-25Cr-1Y alloys were wrapped in Ta foil, vacuum–sealed in quartz capsules, and annealed at 1000°C for 44 min, 2 h 52 min, 8 h 20 min, and 24 h 40 min. Microstructures of the annealed samples were examined by SEM and EDX analysis. Figures 39-41 show SEM photomicrographs of Fe-25Cr, Fe-25Cr-1Ce, and Fe-25Cr-1Y alloys, respectively, in as–fabricated condition and after annealing. In the initial stages of the annealing treatment, grain growth in the base alloy was much greater than in the doped alloys. Figure 42 shows SEM photomicrographs and EDX spectra for surfaces of Ce-containing alloy after the 24 h 40 min annealing treatment. The presence of Ce in the alloy causes the boundaries to be less mobile, leading to smaller grain growth. Figure 43 shows the variation in grain size as a function of annealing time for the base and doped alloys. Lack of grain growth in the substrate alloy is probably the major reason for the better adhesion of the oxide scale to the substrate in the doped alloys.

To examine the effect of alloy grain growth on the scale spallation behavior of Fe-25Cr alloy, specimens of the alloy that had been annealed at 1000°C in vacuum were oxidized in the TGA test facility. Figure 44 shows a comparison of weight change data obtained for the alloy with and without annealing treatment. Also shown in the figure are the data for the second oxidation run in which spalled scale was removed and the specimen was reoxidized. The results show that during the first oxidation experiment, the alloy developed an oxide scale accompanied by substantial grain growth in the substrate alloy. Upon cooling of his oxidized specimen, the scale spalled completely. When the same specimen was reoxidized in the second run, the alloy again developed an oxide scale of essentially the same morphology, but grain growth in the underlying alloy was negligible. This seems to enhance the adhesion of the scale to the substrate, and oxide spallation was rarely observed. Figure 45 shows a cross section of an initially annealed Fe-25Cr alloy that was oxidized at 1000°C; good bonding between the scale and the substrate alloy can be seen.

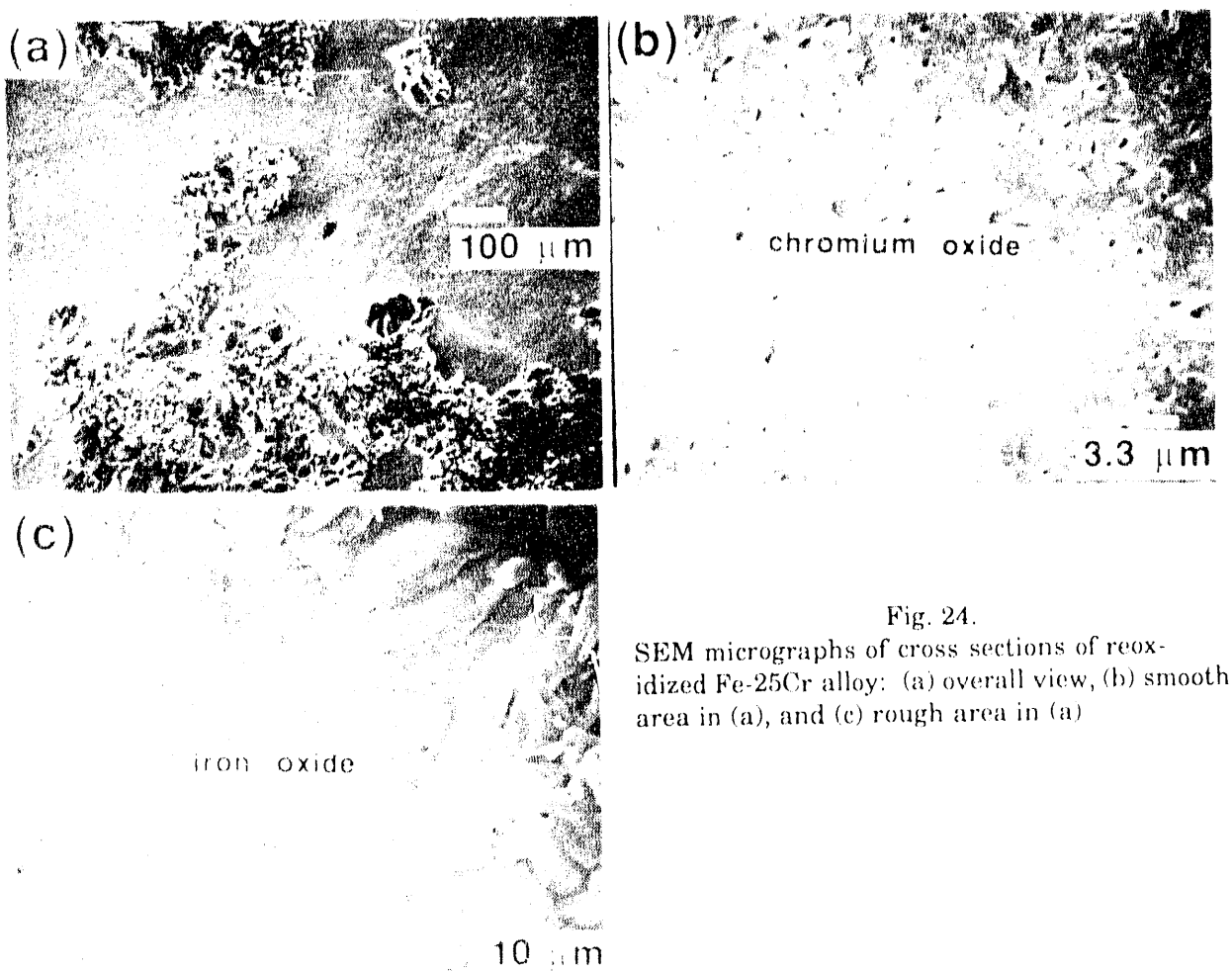

Fig. 24.
SEM micrographs of cross sections of reoxidized Fe-25Cr alloy: (a) overall view, (b) smooth area in (a), and (c) rough area in (a)

Electrical Resistivity Data

Foil samples of Fe-25Cr and Fe-25Cr-1Ce alloys were mechanically polished and cut into coupons (8.9 x 16.5 x 0.05 mm) for use in a four-probe electrical-conductivity measurement. Prior to these measurements, the foils were oxidized (at 1100°C in oxygen) in a TGA facility to achieve complete oxidation. Figure 46 shows the weight change data, which reaches a fixed value in ~80 h, indicating complete oxidation of the foil. The observed weight change and the calculated weight for complete oxidation were in good agreement. Figure 47 shows SEM photomicrographs and an EDX spectrum of the oxide surface and fracture edge. The Cr/Fe ratio near the surface was 0.21, whereas that at the fracture edge ranged from 0.37 to 0.81, indicating that the oxide was enriched in Cr in the latter regime. At the center of the fracture surface, the ratio was 1.3, indicating a Cr-rich oxide. However, these trends varied when reactive elements (Y and Ce) were present in the alloy.[5] Only chromia formed in Y- and Ce-containing alloys when exposed to the same experimental conditions.

Figure 48 shows ohmic resistance as a function of temperature for the oxides prepared by complete oxidation of Fe-25Cr alloy with and without Ce addition at 1083°C in a 100–ppm O_2-N_2 gas mixture. Over the temperature range studied, the oxide of the Ce-containing alloy shows higher ohmic resistance than does the base alloy. These results can be analyzed by the defect–incorporation scheme described below.

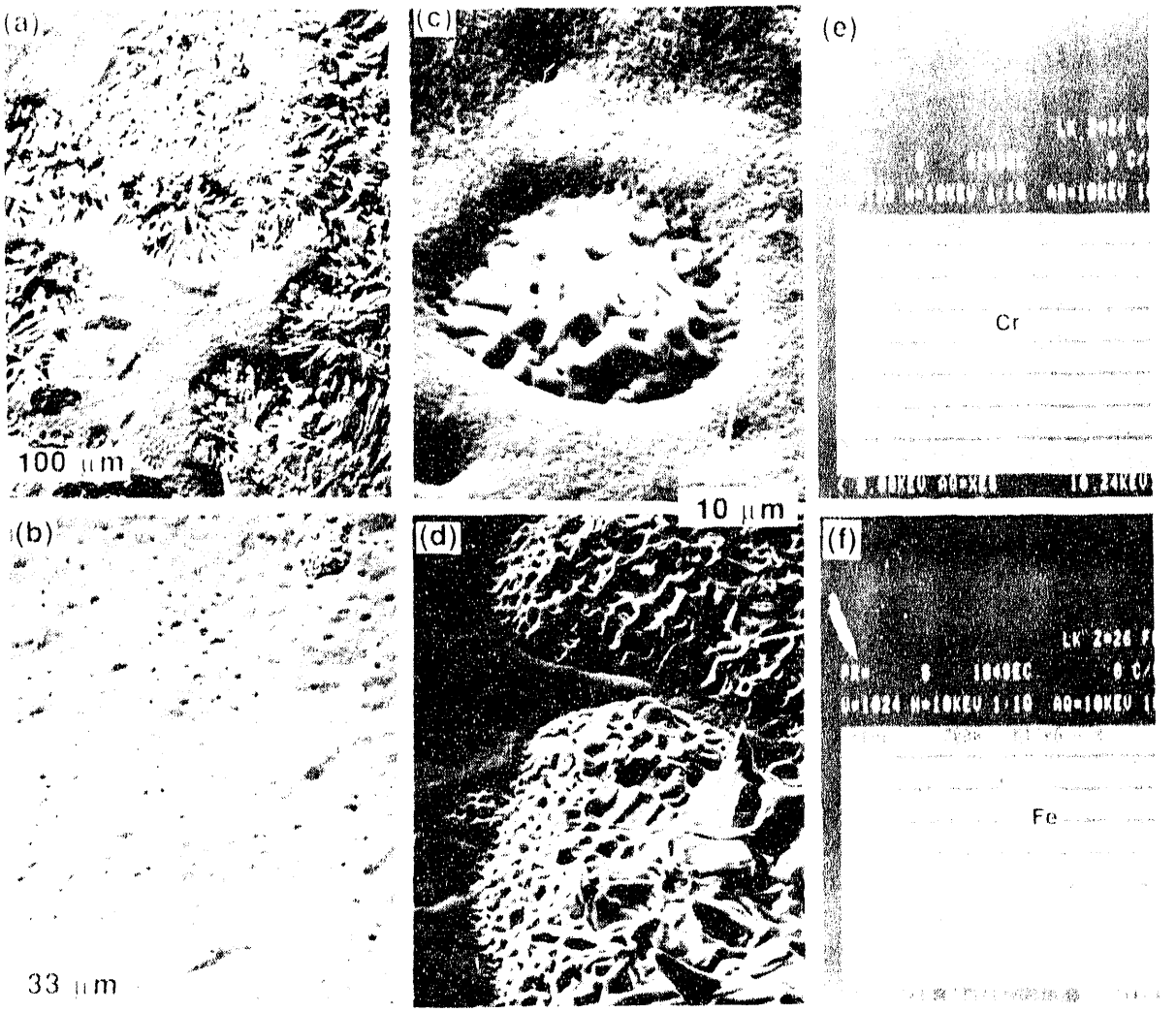

Fig. 25. Details of iron oxide formation during reoxidation of Fe-25Cr alloy: (a)-(d) macro- and micrographs of iron oxide nucleation/growth, (e) and (f) EDX analysis of smooth and nodule regions, respectively

In the high-pO_2 region, the most stable valence state of Ce is +4. When Ce is incorporated into the cation sublattice at either the Cr (+3) or the Fe (+3) site,

$$CeO_2 = Ce^{\bullet}_{Cr(or\ Fe)} + 1/2\ O_2(g) + 3/2\ O^{X}_{O} + e'. \quad (1a)$$

Similarly, when we consider the cation interstitial as a point defect, incorporation of the Ce ion may be written as

$$CeO_2 = Ce^{\bullet\bullet\bullet\bullet}_{i} + 2\ O_2(g) + 4\ e'. \quad (1b)$$

In either case, electrons are produced as a charge-compensating defect. The electron holes are annihilated by recombination with electrons, i.e.,

$$\text{nil} = e' + h^{\bullet}. \quad (2)$$

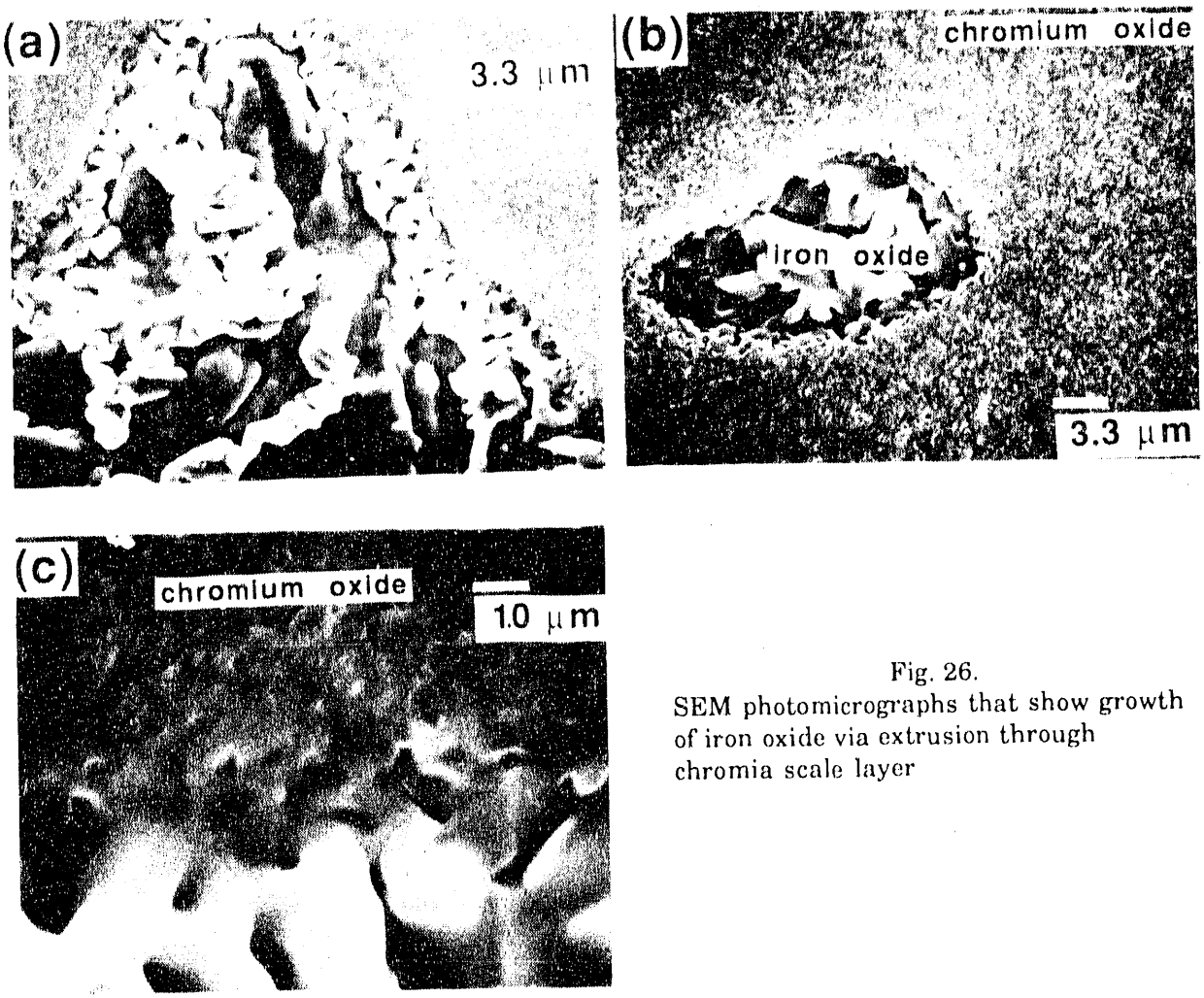

Fig. 26.
SEM photomicrographs that show growth of iron oxide via extrusion through chromia scale layer

As a result, ohmic resistance increases, i.e., electrical conductivity decreases. The studies indicate that Cr_2O_3 is predominantly a p-type semiconductor,[6] as is the oxide developed on Fe-25Cr.

To evaluate the kinetics of mixing of cations (Fe and Cr) in the oxide, ohmic resistance was monitored as function of time and the results are shown in Fig. 49. With the assumptions of a thin–plate model for diffusion and no chemical potential gradient across the oxide sample, diffusivity values were computed. Results are plotted (see Fig. 50) in terms of apparent diffusivity (based on overall thickness of sample) and bulk diffusivity (based on the oxide grain size). Oxygen diffusion data obtained from the literature are also plotted in the figure.[5,26] The results suggest that at high temperatures anion diffusion may contribute to oxidation but at lower temperatures cation diffusion will be the dominant rate–determining factor.

Oxidation Mechanisms

In general, the mechanism of oxidation should incorporate both the thermodynamic and kinetic factors to depict the morphological changes in the scale growing as a function of oxidation time. From the thermodynamic standpoint, oxidation experiments were conducted over a wide

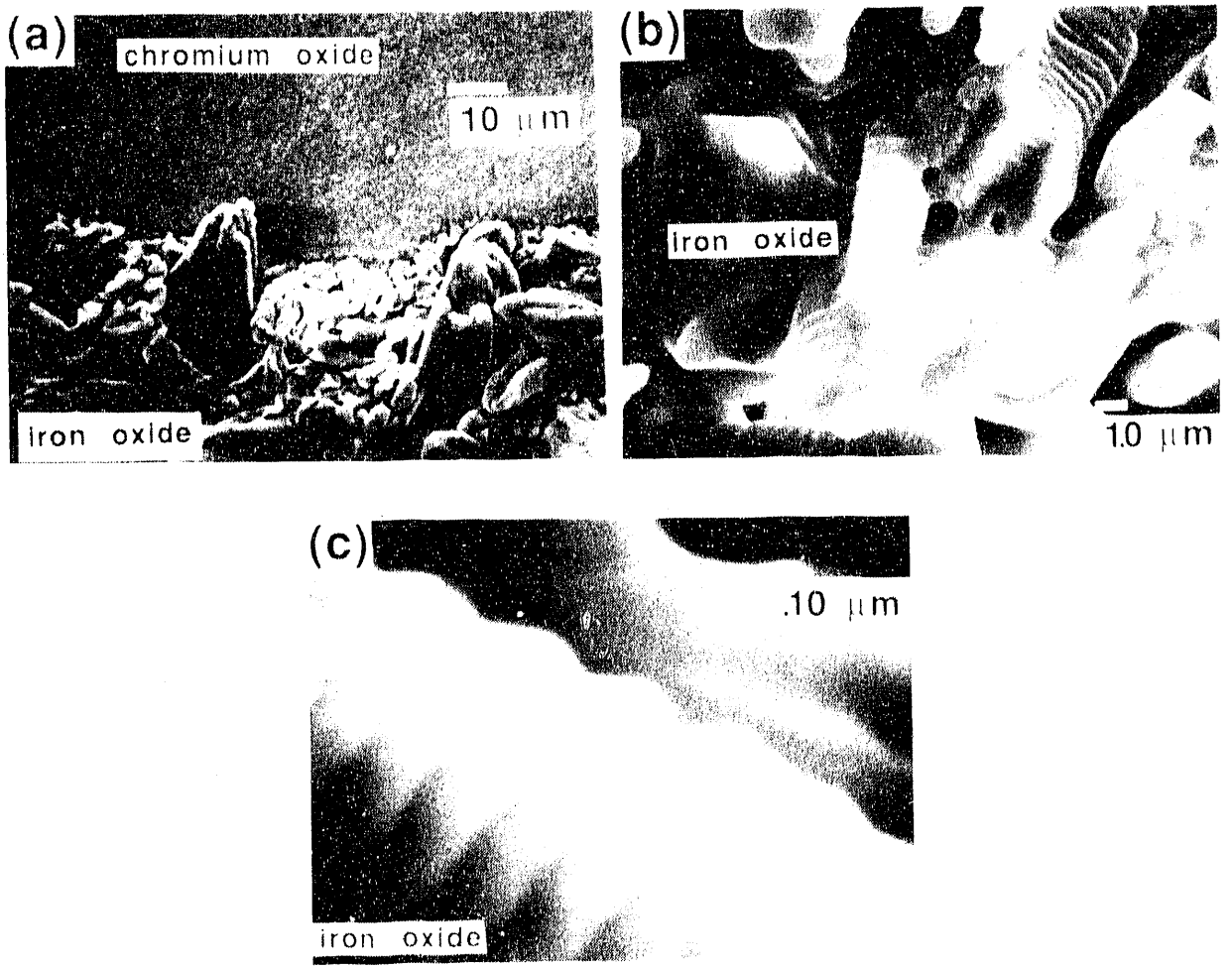

Fig. 27. SEM photomicrographs of pyramid-shaped iron oxide with holes at the top of the pyramids

Table 4. EDS analysis of scale layers developed during oxidation of Fe-25Cr alloy

Scale position	Cation composition
Outer scale	Fe
Outer thin scale	3Fe-97Cr
Outer middle scale	50Fe-50Cr
Inner middle scale	51Fe-49Cr
Inner thin scale	1Fe-99Cr

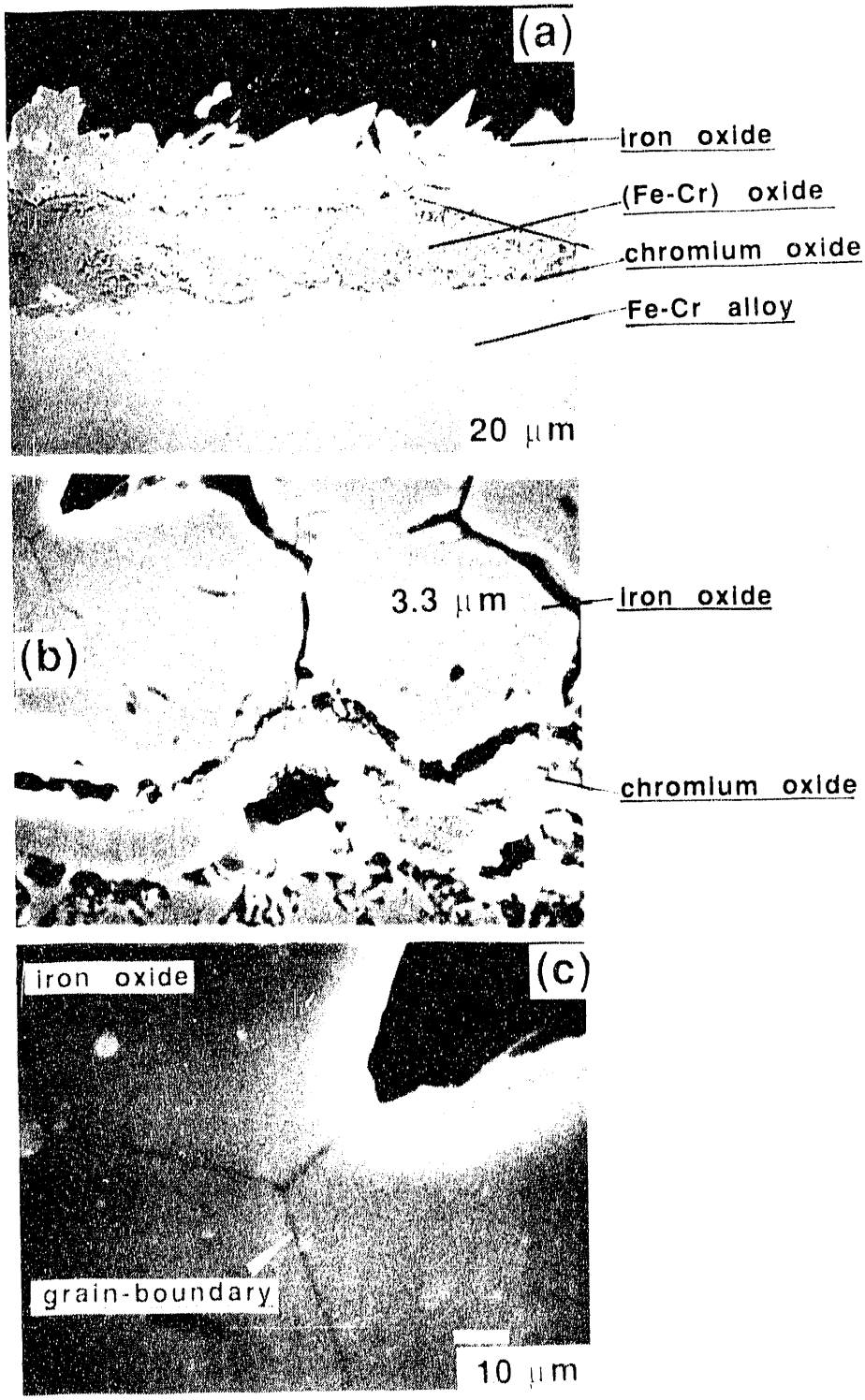

Fig. 28. SEM photomicrographs of cross section of reoxidized Fe-25Cr alloy indicating complex multilayered scale

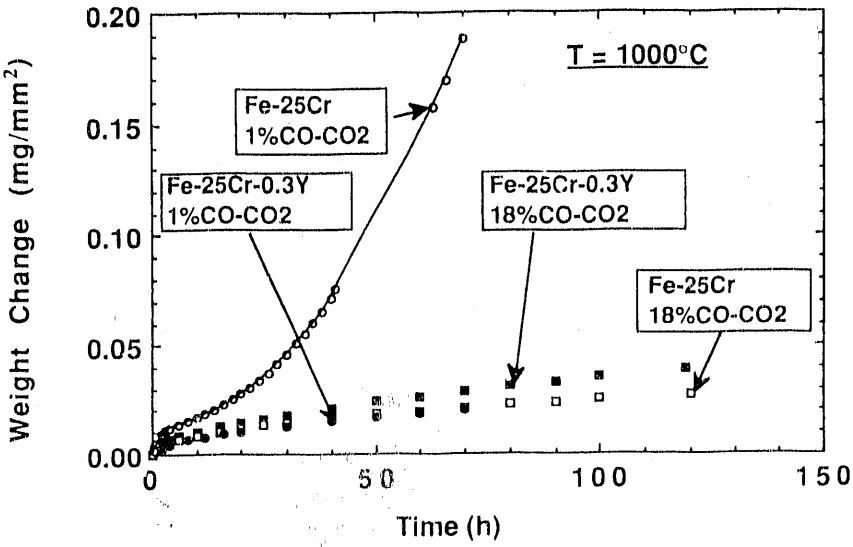

Fig. 29. Weight change versus time for Fe-25Cr and Fe-25Cr-0.3Y alloys exposed at 1000°C in a low-pO_2 environment

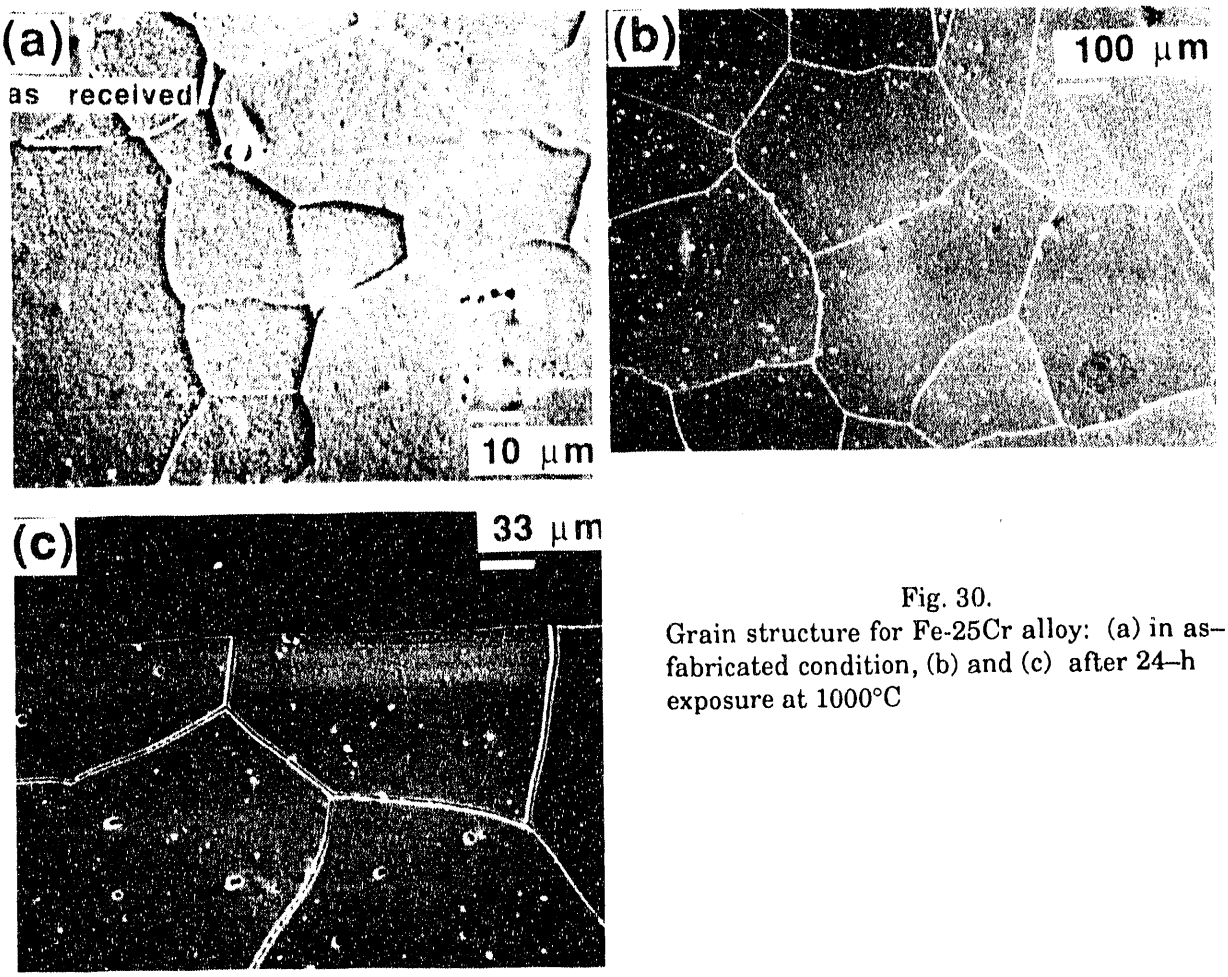

Fig. 30.
Grain structure for Fe-25Cr alloy: (a) in as-fabricated condition, (b) and (c) after 24-h exposure at 1000°C

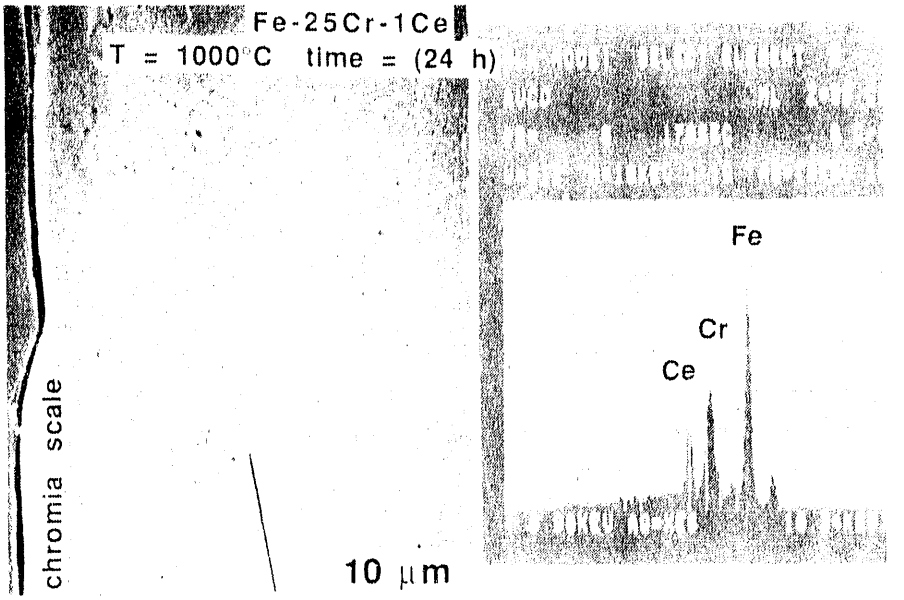

Fig. 31. Cross section of Fe-25Cr-1Ce alloy after 24–h exposure at 1000°C, showing Ce segregation in alloy grain boundaries

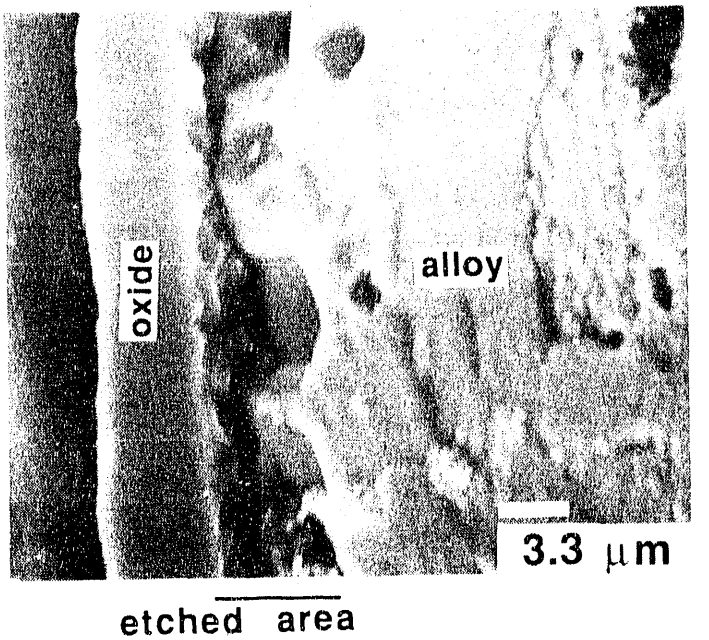

Fig. 32. Grain size and shapes of Fe–25Cr–1Y alloy substrate and oxide scale revealed by etching

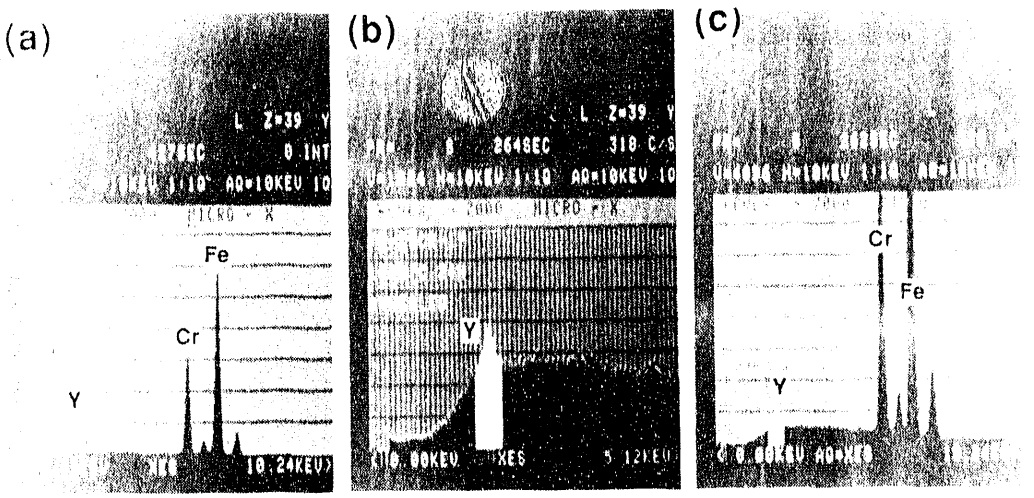

Fig. 33. EDX analysis showing presence of Y in grain boundaries in Fe-25Cr-1Y alloy

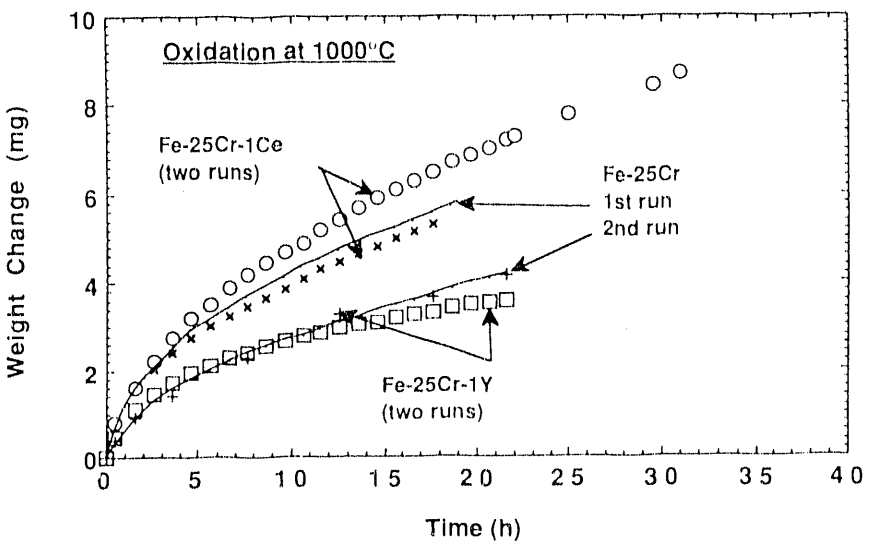

Fig. 34. Thermogravimetric test data for Fe-25Cr, Fe-25Cr-1Ce, and Fe-25Cr-1Y alloys oxidized at 1000°C in a low-pO_2 environment

range of temperatures and pO_2s, and morphologies of scales were determined. From the kinetic standpoint, scale growth and alloy grain growth were examined by oxidation experiments of different times and by establishing the morphological development of scales.

In oxidation of the Fe-25Cr alloy, the mobile species are cations (Cr and Fe) and anion (O). Oxide scale forms and grows by transport of one or more of these mobile species through the scale and subsequent chemical reactions. The oxide growth kinetics and associated morphological development are primarily dependent on the transporting species and their properties. However, it is difficult to determine the transport properties of each and every species because of the influence of scale microstructure, defects, alloy fabrication procedure, and exposure conditions of the oxidation experiment. In this section, oxidation mechanisms are proposed for Fe-25Cr alloys without and with reactive-element additions, based on the results from the present study.

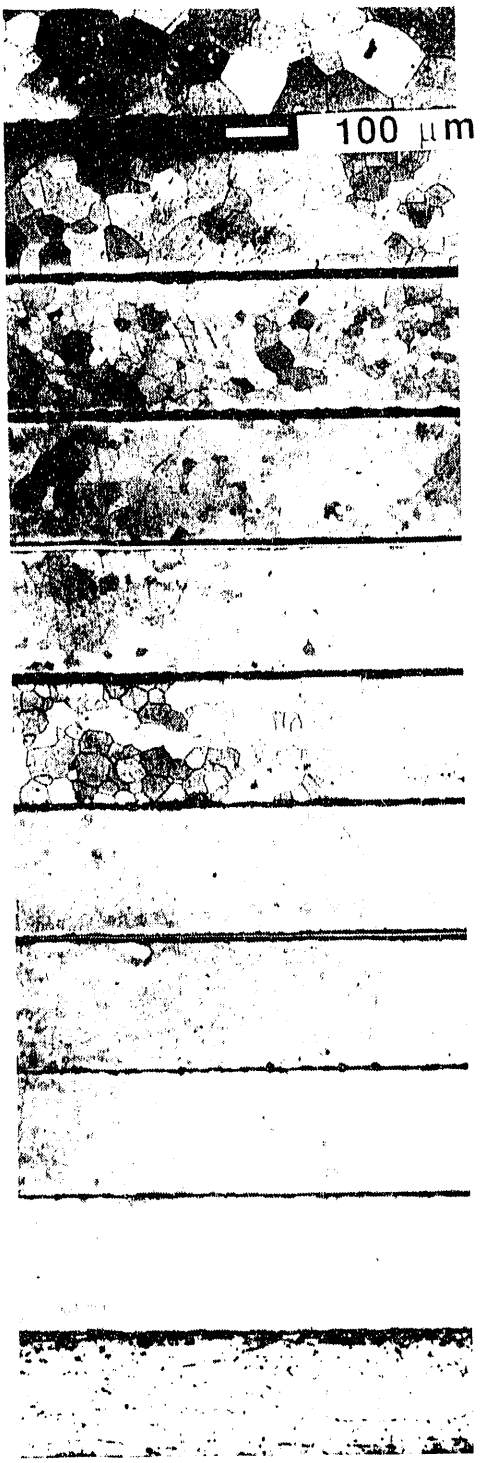

Fig. 35. SEM photomicrographs of Fe-25Cr alloy oxidized at several temperatures and in different environments

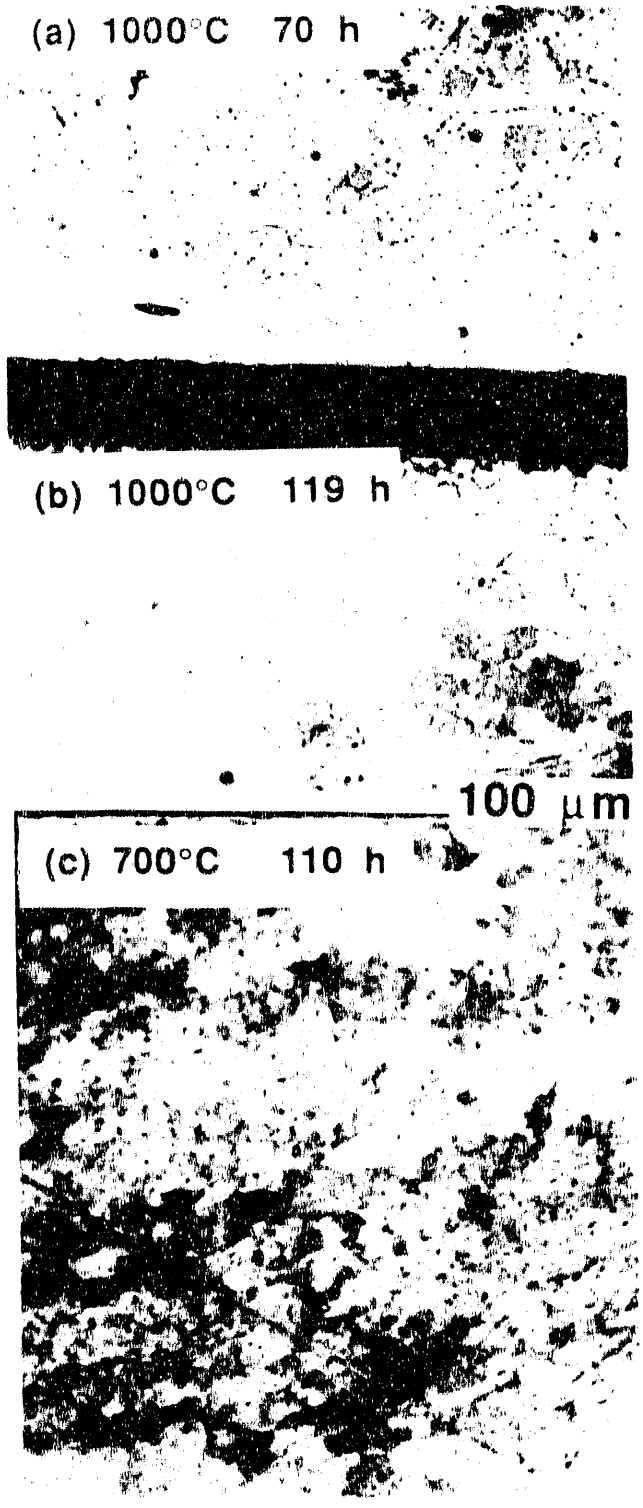

Fig. 36. SEM photomicrographs of Fe-25Cr-0.3Y alloy oxidized at several temperatures and in different environments

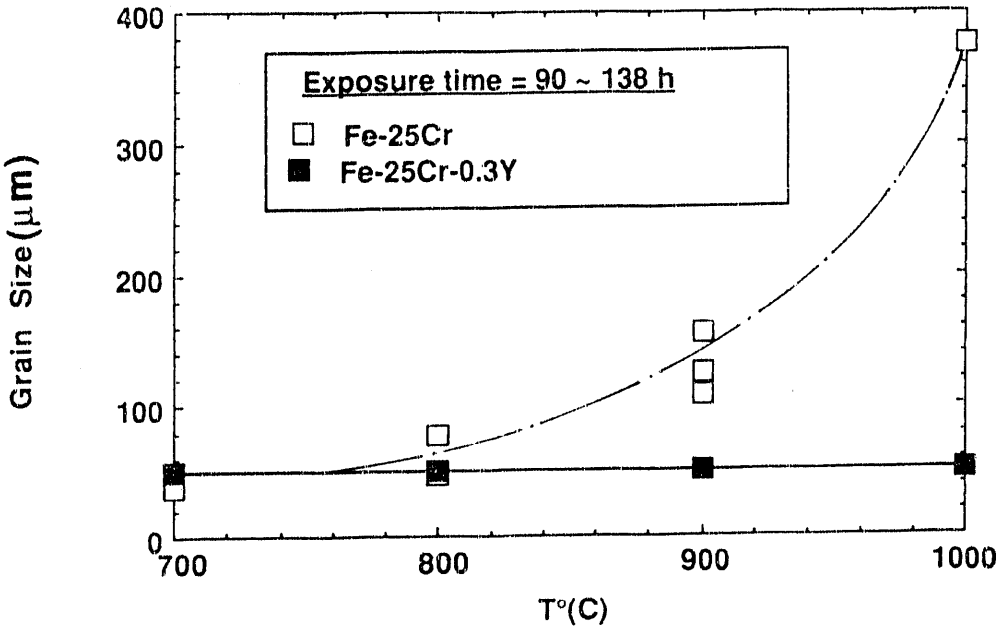

Fig. 37. Grain size variation for Fe-25Cr and Fe-25Cr-0.3Y alloys during oxidation at temperatures from 700 to 1000°C

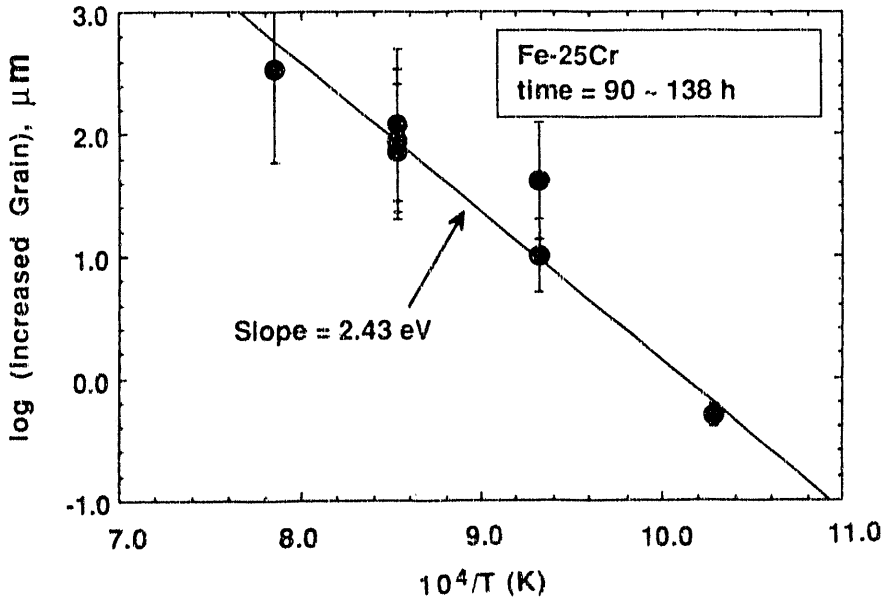

Fig. 38. Temperature dependence of grain size increase for Fe-25Cr alloy

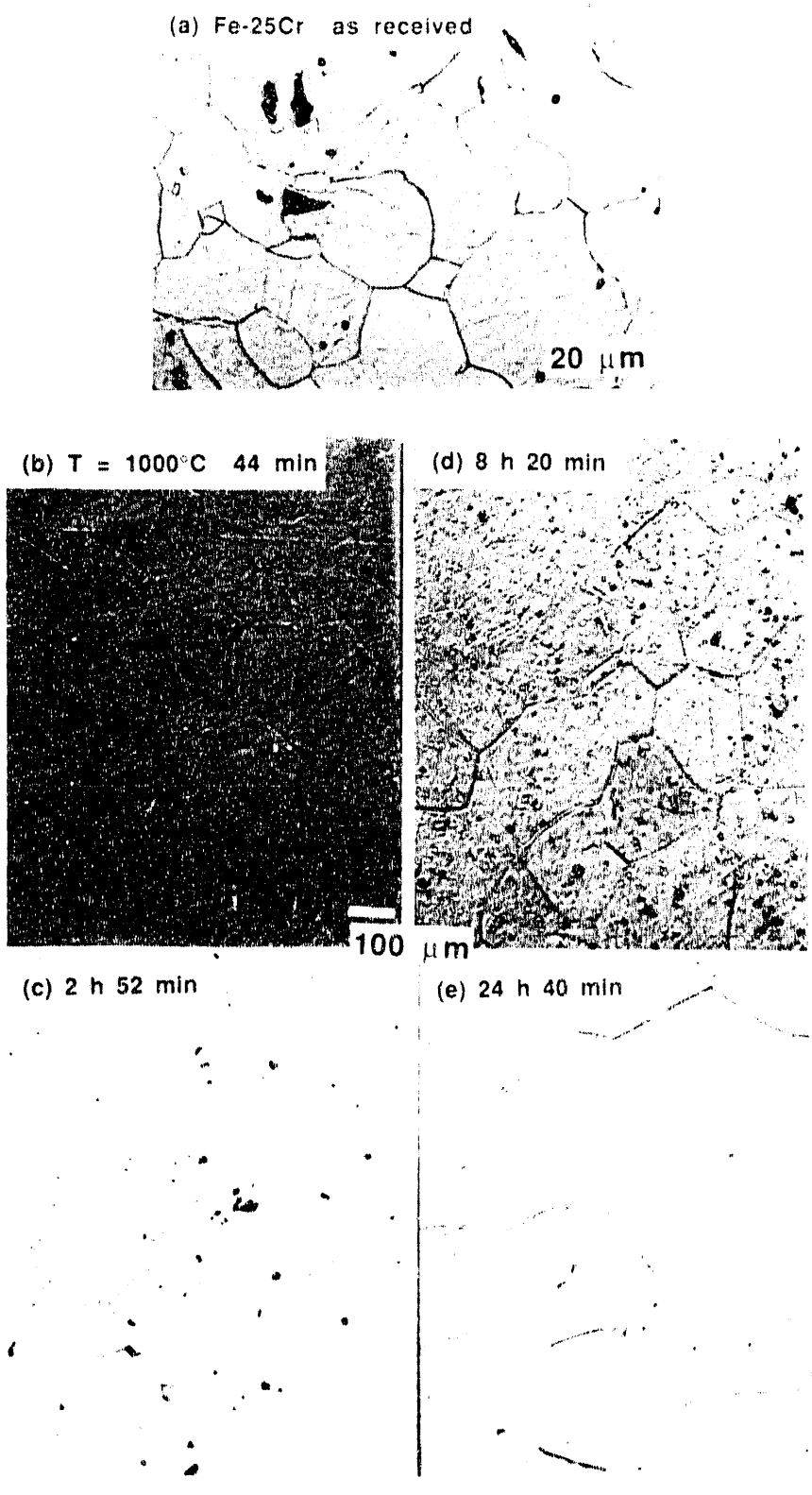

Fig. 39. SEM photomicrographs of Fe-25Cr alloy in (a) as-fabricated condition and after exposure at 1000°C for (b) 44 min, (c) 2 h 52 min, (d) 8 h 20 min, and (e) 24 h 40 min

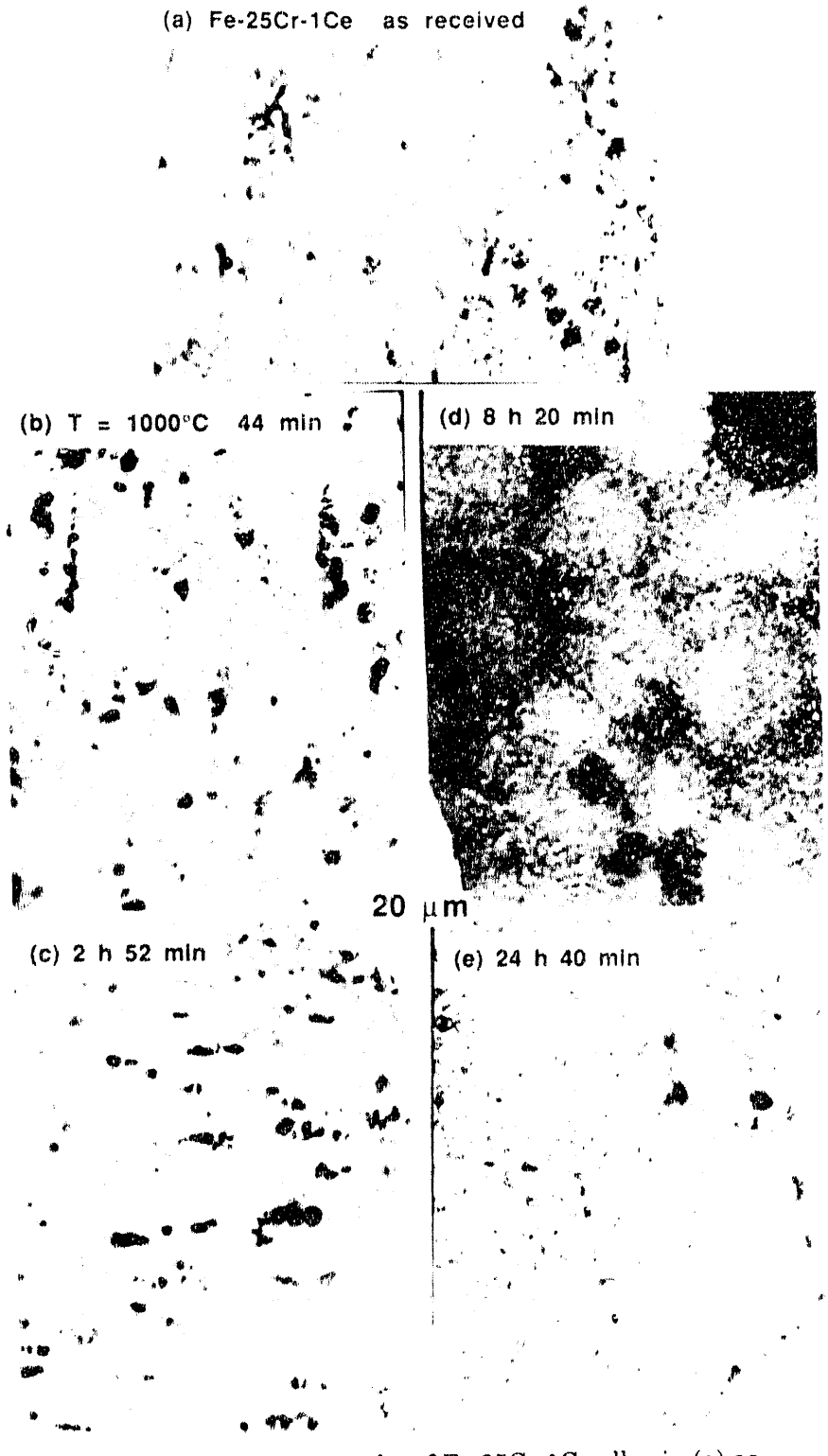

Fig. 40. SEM photomicrographs of Fe-25Cr-1Ce alloy in (a) as-fabricated condition and after exposure at 1000°C for (b) 44 min, (c) 2 h 52 min, (d) 8 h 20 min, and (e) 24 h 40 min

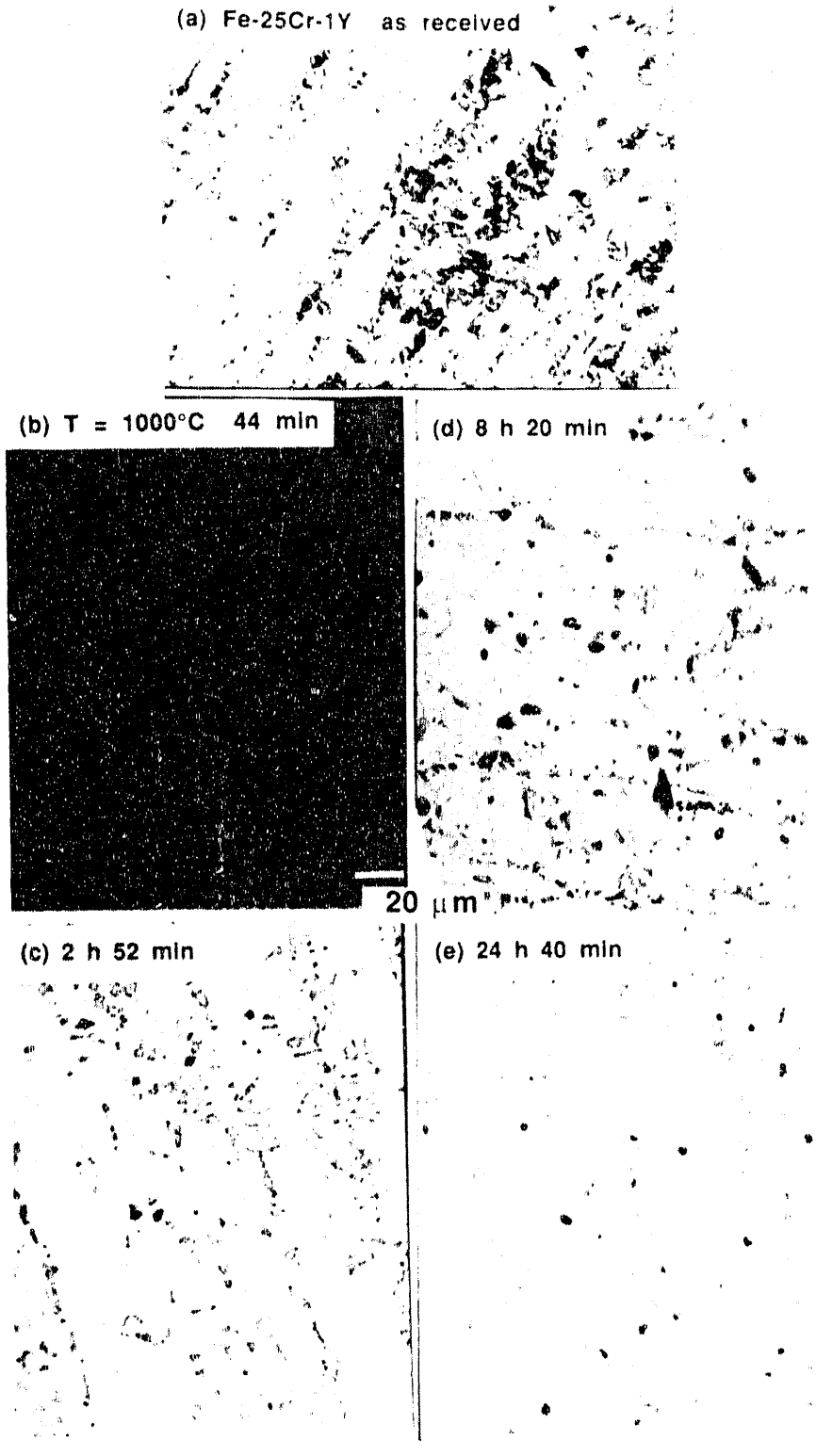

Fig. 41. SEM photomicrographs of Fe-25Cr-1Y alloy in (a) as-fabricated condition and after exposure at 1000°C for (b) 44 min, (c) 2 h 52 min, (d) 8 h 20 min, and (e) 24 h 40 min

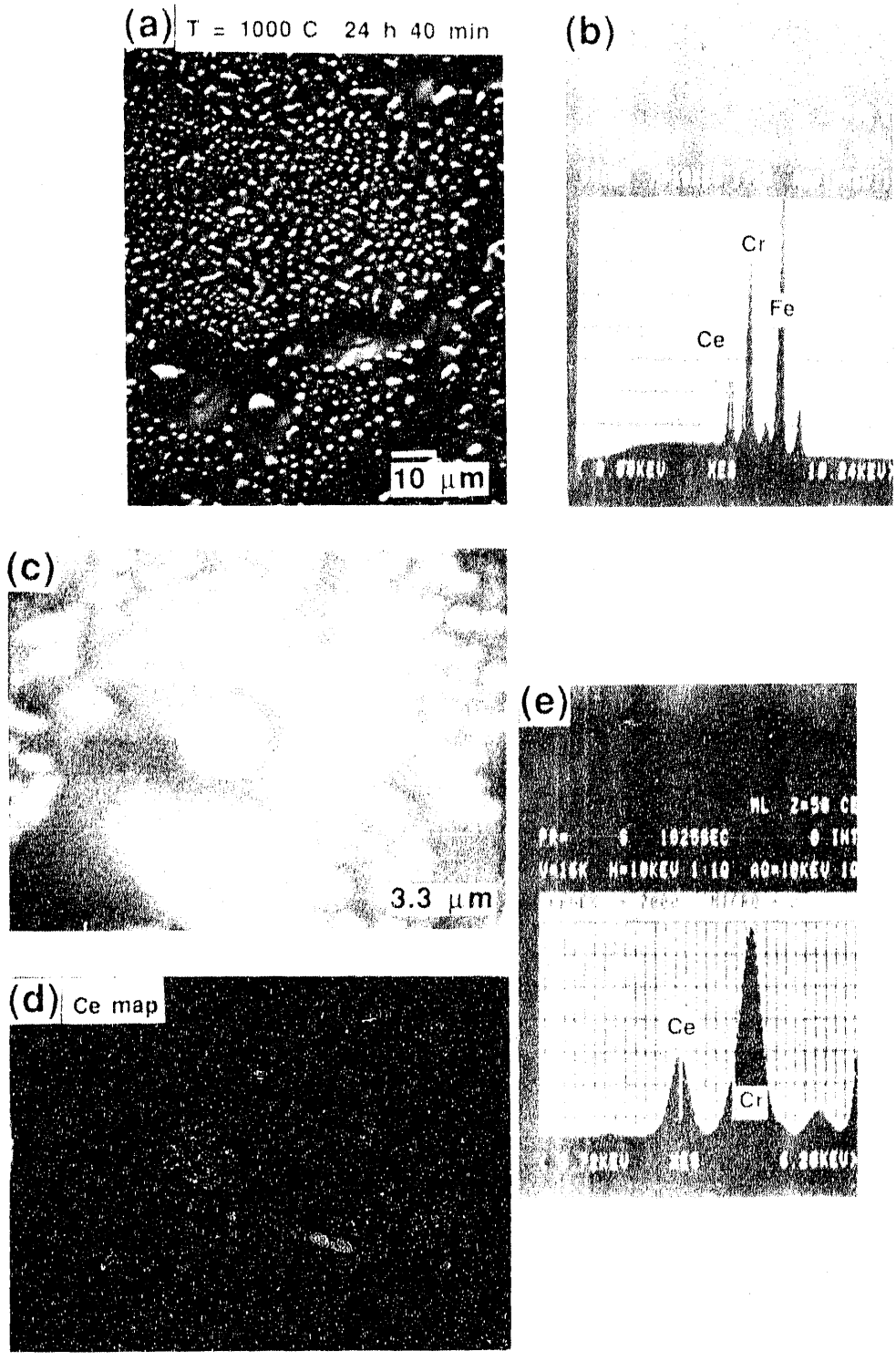

Fig. 42. SEM photomicrographs and EDX analysis of Fe-25Cr-1Ce alloy annealed for 24 h 40 min at 1000°C

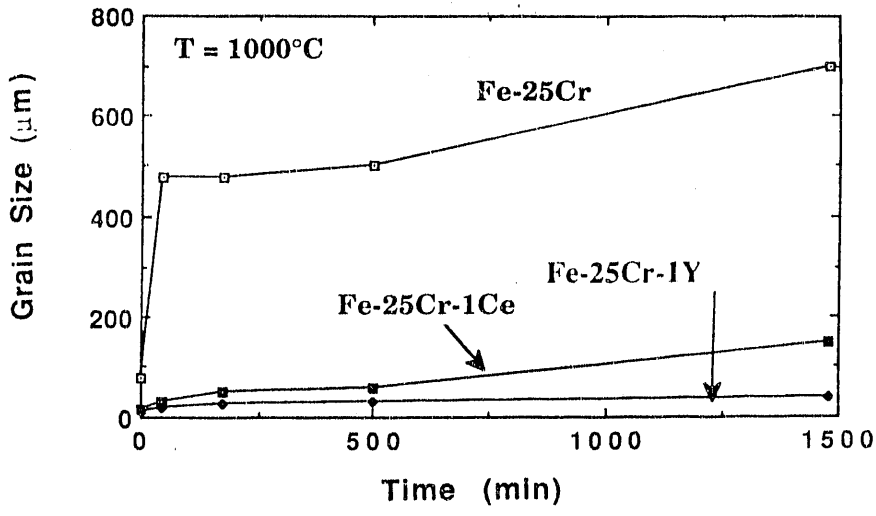

Fig. 43. Comparison of grain–size variation in Fe-25Cr, Fe-25Cr-1Ce, and Fe-25Cr-1Y alloys as a function of exposure time

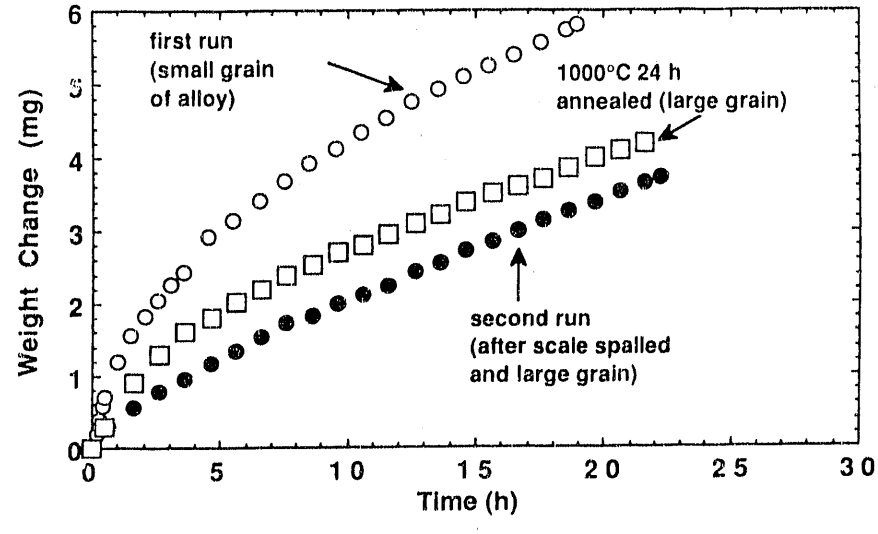

Fig. 44. Weight change versus time at 1000°C for oxidation of Fe-25Cr alloy with different initial treatments

Without Reactive Element

First Oxidation. When a specimen of Fe-25Cr alloy was oxidized at 1000°C for 24 h and quenched to room temperature, separation of scale from substrate alloy resulted in total spallation of the scale. The primary cause of the separation seemed to be grain growth in the underlying alloy during oxidation. From the beginning of oxidation, a thin chromia scale formed on the specimen surface. Based on thermodynamics, chromia is expected to form due to its higher stability than that of iron oxide. As the oxidation continued, chromia scales grew in a wavy and partially folded fashion. In the early stages of oxidation, the scale was thin and completely covered the alloy surface. The scale/alloy interface was fairly uniform, and adhesion of the scale to the substrate was good. As oxidation continued, grain growth in the substrate alloy caused the oxide to separate from the alloy at several locations; this separated oxide buckled and appeared wavy in cross section (see schematic in Fig. 51a). The scale exhibited only a few points of contact with the

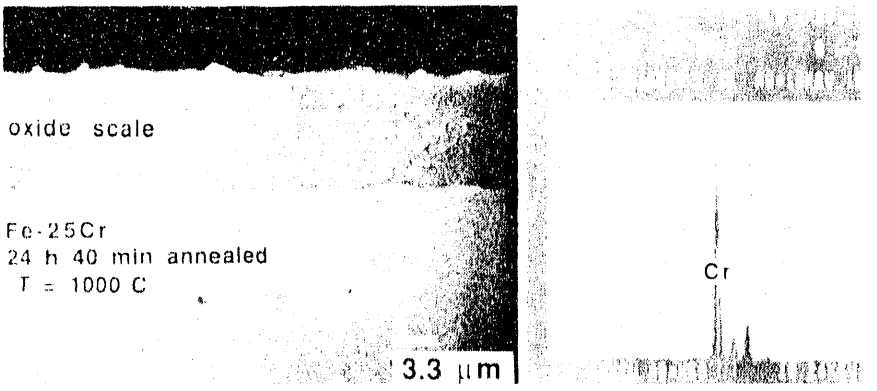

Fig. 45. SEM photomicrograph of cross section of initially annealed Fe-25Cr alloy after oxidation at 1000°C

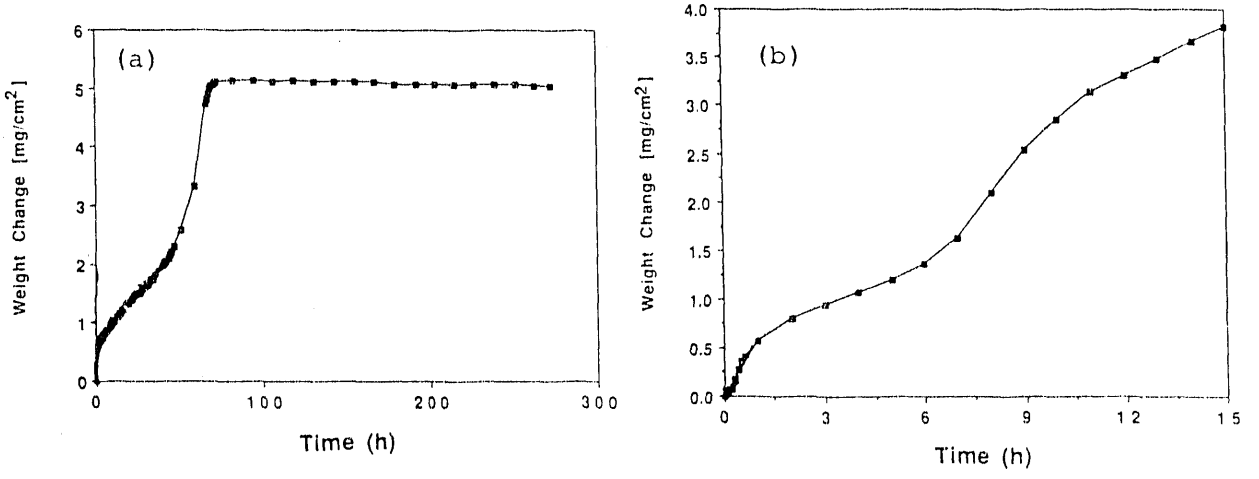

Fig. 46. Thermogravimetric test data for Fe-25Cr foil sample oxidized at 1100°C in oxygen: (a) oxidation in entire cross section and (b) early stage of oxidation

substrate alloy and adhesion to the substrate was tenuous at best. When the sample was quenched to room temperature, the scale spalled, primarily because of the mechanical weakness of the buckled scale.

Thermal expansion mismatch may have also contributed to scale spallation but is not the primary cause of the scale failure. Lack of cracks in the scale also indicates that the scale had mostly separated from the alloy during oxidation rather than on cooling from the oxidation temperature. Separation distance between the scale and the underlying alloy was ≈1 μm. Figure 51b is a schematic of the surface of the alloy side of the scale/alloy interface. The grain structure of the base alloy is evident but the surface also exhibits a thin layer of oxide. Figure 51c is a schematic of the cross section of the sample taken along a plane "O" in Fig. 51b.

Second Oxidation. After removal of the spalled oxide from the sample, the specimen (with a thin chromia layer) was reoxidized under the same conditions as in the initial oxidation experiment. The second oxidation was also conducted for 24 h at 1000°C and the sample was quenched to room temperature. Figure 52 shows a schematic of the cross section of the specimen after the

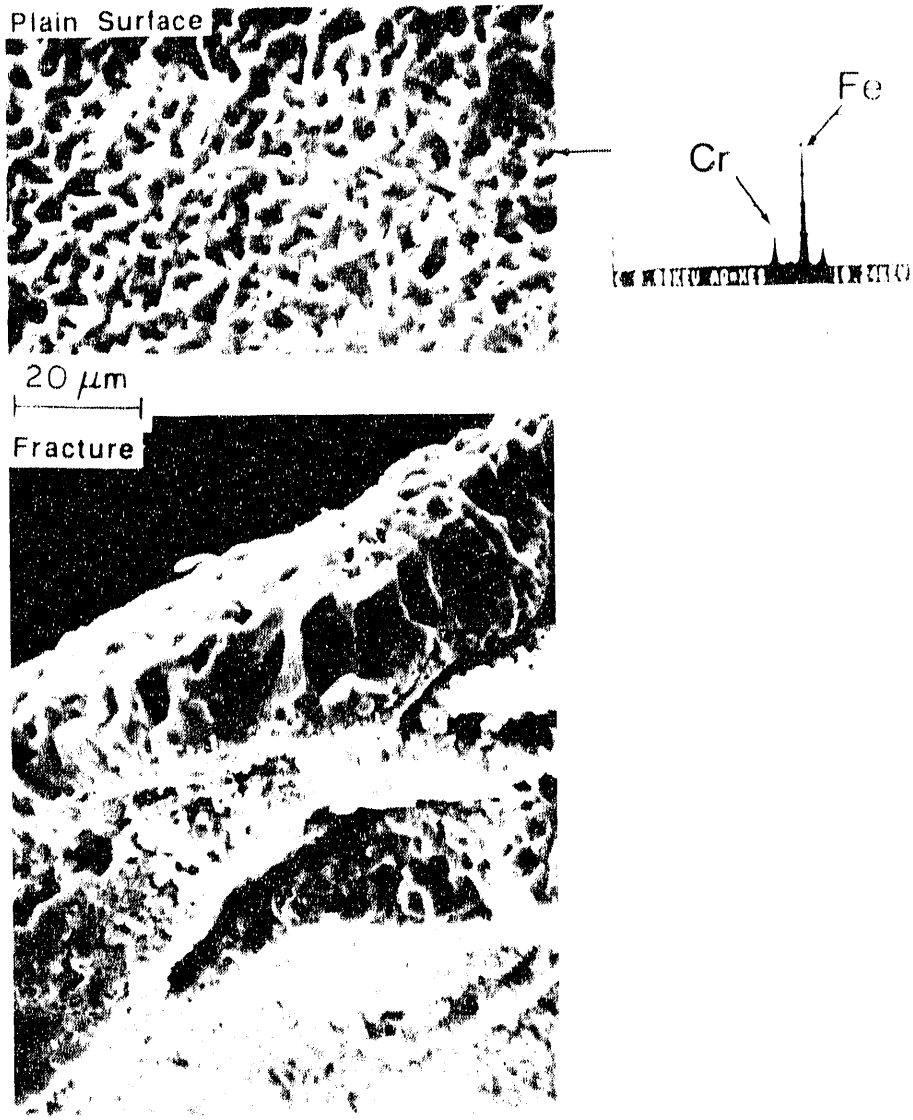

Fig. 47. SEM photomicrographs of surface and fracture cross section of Fe-25Cr alloy and an EDX spectrum of the oxide surface

second oxidation. The thin layer of chromia left behind after scale spallation (from the first oxidation run) did not prevent Fe migration outward from the alloy. In addition, Cr activity at the surface (for the second oxidation run) is much less and the Fe activity is high relative to the unexposed alloy. The migrated Fe oxidized on the gas side of the interface, while an intermediate layer of (Fe,Cr) oxide and a chromia layer developed at the alloy/scale interface. Even though the morphology of the scale layers that developed after the second oxidation was complex and thicker than that after the first oxidation run, scale adhesion to the substrate was extremely good. The superior adhesion and lack of spalling can be attributed to negligible grain growth in the substrate alloy after the second oxidation.

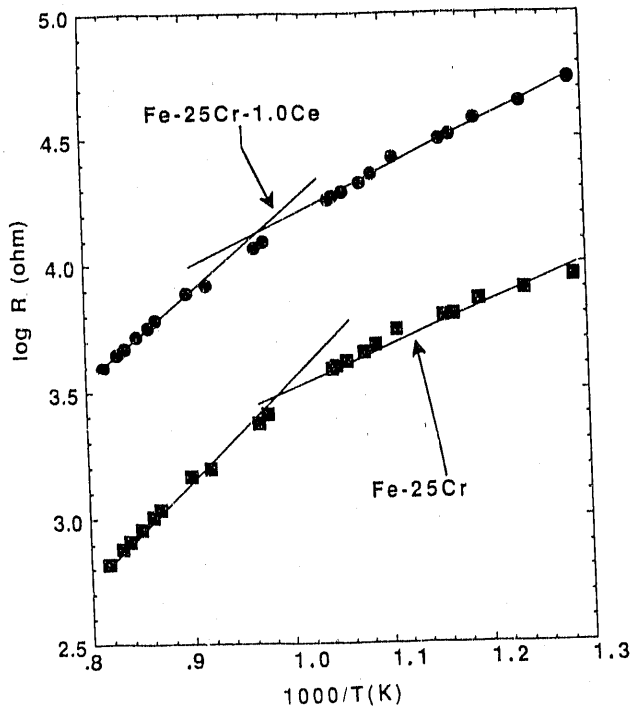

Fig. 48.
Variation in ohmic resistance as a function of exposure temperature for oxidized foil samples of Fe-25Cr and Fe-25Cr-1Ce

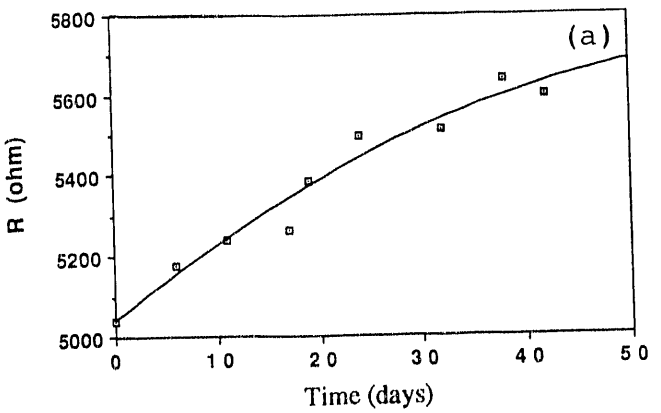

Fig. 49.
Variation in ohmic resistance and calculated diffusivity values as function of exposure time for Fe-25Cr alloy at 714°C

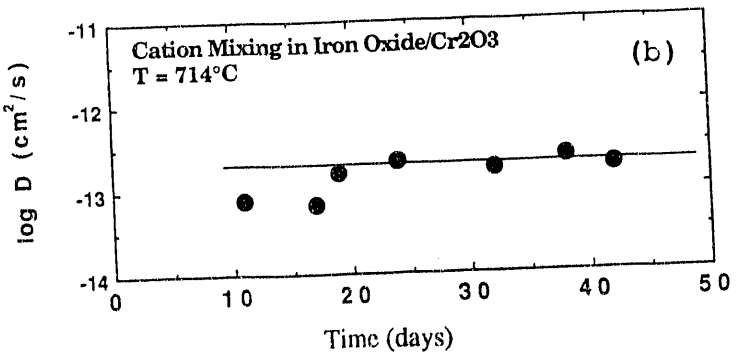

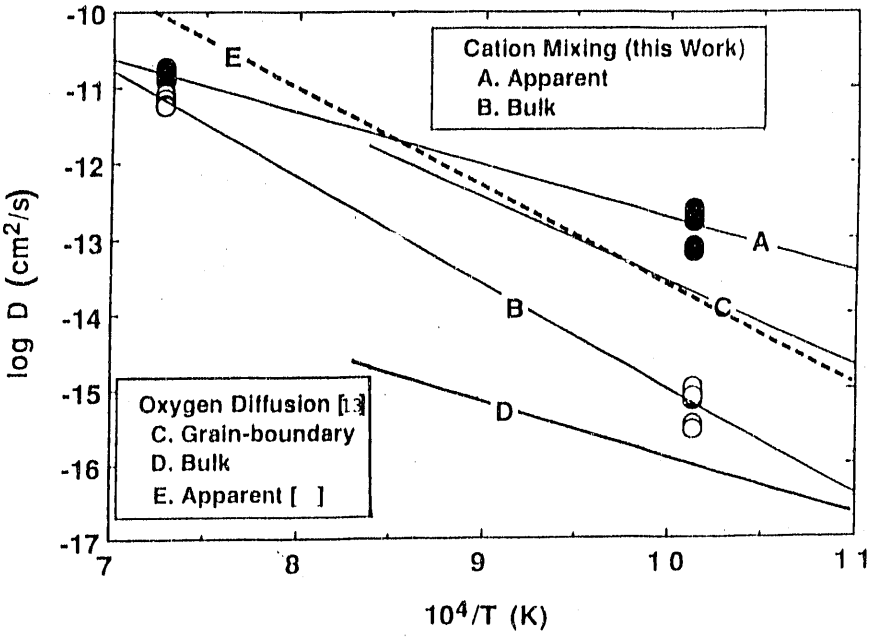

Fig. 50. Temperature dependence of diffusivity of cation and oxygen in thermally grown oxide scales in chromium and Fe-25Cr alloy

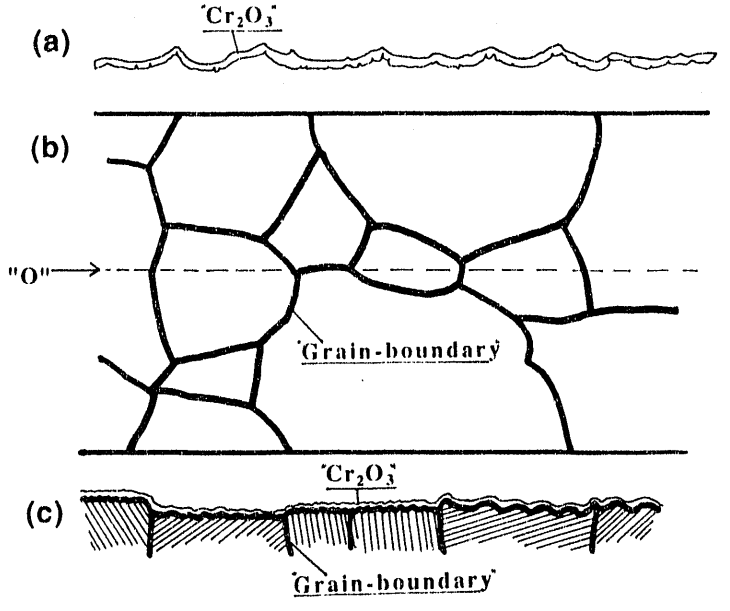

Fig. 51. Schematic representation of oxidation of Fe-25Cr alloy: (a) chromia scale totally spalled (b) alloy side of scale/alloy interface after spallation, and (c) cross section of specimen at plane "O" shown in (b)

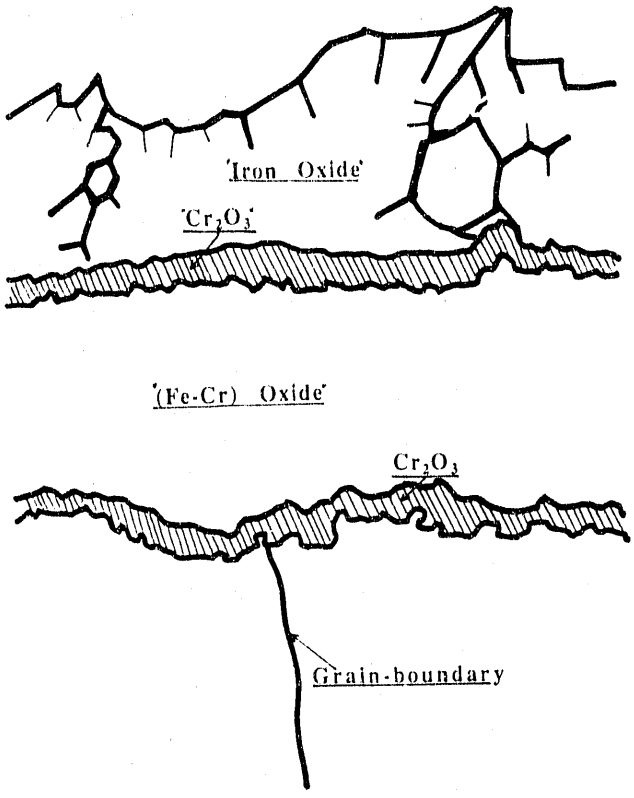

Fig. 52.
Schematic representation of scale morphology developed during reoxidation of Fe-25Cr alloy at 1000°C

With Reactive Element

Oxidation of alloys containing reactive elements at 1000°C for 24 h exhibited negligible difference in the rate of oxidation; however, the additions had some beneficial effect over longer oxidation periods (>120 h at 1000°C). The composition of the scale in the reactive-element–containing alloys was pure chromia, and no trace of Fe was detected in the scale. Morphological analysis of scale layers indicated that Fe diffusion outward is suppressed in these doped alloys. There is some evidence, even though not conclusive in this study, that O transport inward may also contribute to scale growth. Parabolic rate constants for oxidation of the doped alloys were similar to those for undoped alloys. The major difference in the performance of the doped and undoped alloys is in scale adhesion. Adhesion was much superior in the doped alloys and virtually no spallation of scale was observed, even under thermal quenching. The improved adhesion can be attributed to smaller grain growth in the doped alloys than in undoped alloy.

Figures 53 and 54 show schematics of scale morphologies in Ce- and Y-containing alloys after oxidation. These doped alloys developed pure chromia scales at high temperatures and the dopants had a tendency to oxidize internally and to segregate in grain–boundary regions of the substrate alloy. The presence of these internally oxidized particles seems to pin the grain boundaries, thereby minimizing grain growth in the substrate alloy during oxidation. Lack of grain growth in the alloy results in improved adhesion of the scale to the substrate and virtual elimination of scale spallation, even after thermal quenching. Of the two dopants used in the present study, Y seems better than Ce because the Ce-containing alloys exhibited much higher weight gain, primarily due to increased internal oxidation. Further, Ce can combine with Fe to form a low-melting (640°C) eutectic that decreases oxidation resistance.

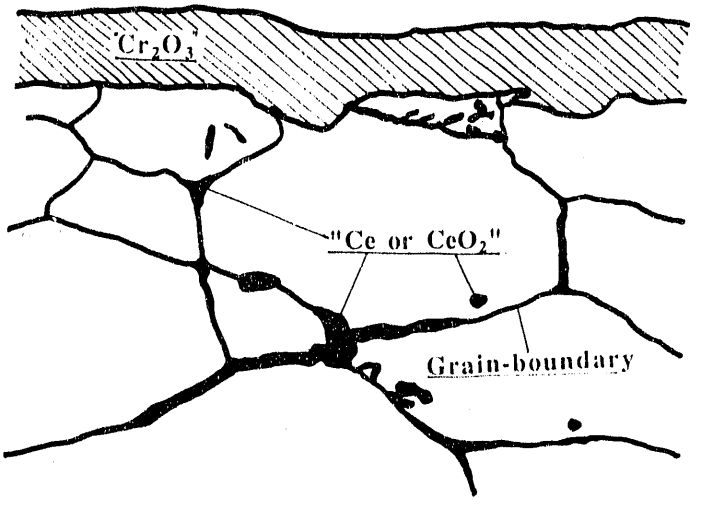

Fig. 53. Schematic representation of scale morphology developed during oxidation of Fe-25Cr-1Ce alloy at 1000°C

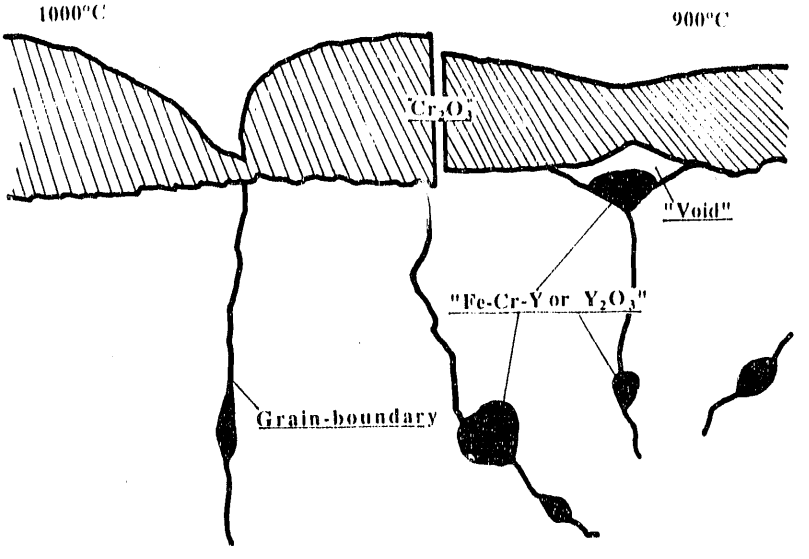

Fig. 54. Schematic representation of scale morphology developed during reoxidation of Fe-25Cr-1Y alloy at 1000°C

SUMMARY

Alloy samples of Fe-25Cr, Fe-25Cr-0.3 and 1.0Y, and Fe-25Cr-1Ce were subjected to oxidation tests in a microbalance at temperatures of 700 to 1000°C for time periods of 24 to 120 h in pO_2 ranging from 10^{-4} to 1 atm. Tests were also conducted in which oxidized samples were quenched from oxidation temperature to room temperature in ≈20 min. Thermal quenching test results showed total spallation of oxide scale from Fe-25Cr alloy while no spallation was observed in Y- and Ce-doped alloys. After removal of the spalled oxide, the Fe-25Cr alloy specimen was reoxidized a second and third time with the same procedure used in the first oxidation run. Test results showed substantial improvement in adhesion of the scale to substrate after these

runs; however, the totally spalled scale from the first run was pure chromia while that after the second and third runs comprised a multilayer scale with iron oxide as the dominant phase at the gas/scale interface. Even though the scale thickness after the repeated oxidations was somewhat thicker than during the first oxidation, the oxidation resistance of the alloy seems to have improved.

The primary cause for scale spallation is identified as grain growth in the alloy substrate during the oxidation process. The extent of grain growth during the first oxidation step was substantially larger than in the following oxidation steps. Additions of reactive elements such as Y and Ce seem to pin the grain boundaries in the substrate alloy, thereby minimizing grain growth even during the first oxidation step. As a result, Y- and Ce-doped alloys developed pure chromia scales that were resistant to spallation and exhibited superior oxidation resistance even under thermal quenching.

To examine the effect of reactive–element additions on alloy grain growth, specimens with and without alloying additions were annealed in an inert atmosphere (to prevent oxidation) for different time periods. Postexposure analysis of the specimens was performed to determine the grain–growth kinetics. After a 40–min anneal at 1000°C, the grain size of the Fe-25Cr alloy showed a tenfold increase, while the grain size of the doped alloys increased by <1%. Segregation of Y and Ce in alloy grain boundaries (more in Ce– than in Y–containing alloys) was observed. The Ce-containing particles seemed to coalesce as a function of annealing time but prevented grain growth in the substrate alloy. As a result, the doped alloys exhibited good adhesion between scale and substrate and no scale spallation was observed.

Additional experiments were conducted to evaluate the role of grain size and grain growth on the spallation characteristics of thermally grown oxide scales. Fe–25Cr alloy specimens were oxidized at 1000°C and the scale, even though thin and with a composition of pure chromia, spalled totally. The grain size of the substrate alloy increased tenfold during oxidation exposure. The same specimen (after removal of spalled scale) was reoxidized a second and third time with the procedure used in the first run. The scales that grew were somewhat thicker and the morphology was complex, with pure iron oxide at the gas side of the interface; however, adherence of the oxide scale to the substrate was very good and no scale spallation resulted. The grain size of the substrate alloy grew tenfold between the first step and the subsequent oxidation steps. Grain–growth rate during the first oxidation step was ten times that of the starting size in 24 h, while that in subsequent steps was 1% in 24 h. These results suggest that starting grain size of the substrate alloy has a negligible effect on adhesion properties and spallation characteristics of thermally grown oxide scales, while substrate–alloy grain growth (which occurs during oxidation) has a significant effect on scale retention and high–temperature oxidation resistance of the alloy.

ACKNOWLEDGMENTS

The authors acknowledge the Mechanics of Materials Section of the Materials and Components Technology Division at Argonne for its assistance in the fabrication of the alloys. D. L. Rink assisted in the corrosion tests and microstructural analysis of the exposed specimens.

REFERENCES

1. K. Natesan, Oxidation of Alloys in Bioxidants, Proc. Symp. Oxidation of Metals and Associated Mass Transport, eds. M. A. Dayananda, S. J. Rothman, and W. E. King, TMS-AIME, Orlando, FL, October 6-7, 1986, p. 161.

2. P. Kofstad, High Temperature Corrosion (Elsevier Applied Science, England, Essex, 1988); Nonstoichiometry, Diffusion and Electrical Conductivity in Binary Metal Oxides, Wiley Interscience, New York, 1972.

3. A. Rahmel, G. C. Wood, P. Kofstad, and D. L. Douglass, International Workshop on Critical Issues Concerning the Mechanisms of High-Temperature Corrosion, Oxid. Metals, 23 (5/6) 251, 1985.

4. L. B. Pfeil, Improvements in Heat Resistant Alloys, Brit. Pat. No. 459848, 1937.

5. J.-H. Park and K. Natesan, Transport Properties of Chromium and Fe-Cr Alloys Exposed to Oxygen/Sulfur Environments, Proc. Fourth Berkeley Conf. on Corrosion-Erosion-Wear of Materials at Elevated Temperatures, January 31-February 2, 1990, Berkeley, CA, NACE.

6. J.-H. Park and K. Natesan, Electronic Transport in Thermally Grown Cr_2O_3, Oxid. Metals, 33(1/2) 31, 1990.

7. L. B. Pankratz, Thermodynamic Properties of Elements and Oxides, NBS 672, Minerals and Materials Research, Bureau of Mines, U. S. Dept. of Interior, Washington, DC, 1983.

8. T. F. Kassner, L. C. Walters, and R. E. Grace, Proc. Symp. Thermodynamics with Emphasis on Nucl. Mater. Atomic Transport in Solids p. 357, I.A.E.A., Vienna, 1966.

9. K. Hoshino and N. L. Peterson, Cr Tracer Diffusion in Cr_2O_3, J. Am. Ceram. Soc. C112, 1984.

10. L. C. Walters and R. E. Grace, Self Diffusion of ^{51}Cr in Single Crystals of Cr_2O_3, J. Appl. Phys. 36(8), 2331, 1965.

11. A. Atkinson and R. I. Taylor, Cr Tracer Diffusion in Cr_2O_3, NATO ASI Ser., B, 129, 285, 1984.

12. J.-H. Park, W. E. King, and S. J. Rothman, Cation grain-boundary diffusion in Cr_2O_3 and Cr_2O_3 doped with Y_2O_3, J. Am. Ceram. Soc. 70, 880, 1987.

13. R. Dieckmann, Diffusion of Cations and of Point Defects in Magnetite, Proc. Symp. Metall. Soc. AIME and MSD-ASM Atomic Transport Activity, TMS-AIME Fall Meeting, Orlando, FL, Oct. 6-7, 1986, p. 7.

14. R. A. Rapp, The High–Temperature Oxidation of Metals Forming Cation–Diffusing Scales, Metall. Trans. A, 15 765,1984.

15. G. M. Raynaud and R. A. Rapp, In–situ Observation of Whiskers, Pyramids, and Pits During the High–Temperature Oxidation of Metals, Oxid. Metals, 21, 89,1984.

16. D. A. Voss, E. P. Butler, and T. E. Mitchell, The Growth of Hematite Blades During the High–Temperature Oxidation of Iron, Metall. Trans. A 13, 929, 1982.

17. W. E. King, N. L. Peterson, and J. F. Reddy, Study of the 'Reactive–element' Effect in Oxidation of Fe–Cr Alloys Using Transverse Section Analytical Electron Microscopy, J. Physique, 46, C4-423, 1985.

18. K. Przybylski, A. J. Garratt-Reed, and G. J. Yurek, Observation of Coherent Provskite Particles in Growing Chromia Films, J. Amer. Ceram. Soc.,69, C-264,1986

19. W. E. King and J.-H. Park, Argonne National Laboratory, unpublished information, 1988.

20. K. Przybylski, A. J. Garratt-Reed, and G. J. Yurek, Grain-boundary segregation of Yttrium in Chromia Scale, J. Electrochem. Soc., 135, 509, 1988.

21. K. Przybylski and G. J. Yurek, The Influence of Implanted Yttrium on the Mechanisms of Chromia Scales, Mat. Sci. Forum, 43, 1, 1989.

22. L. S. Darken and R. W. Gurry, Physical Chemistry of Metals, McGraw-Hill, New York, 1953.

23. A. G. Evans and R. M. Cannon, Stresses in Oxide Film and Relationship with Cracking and Spalling, Proc. Symp. Metall. Soc. AIME and MSD-ASM Atomic Transport Activity, TMS-AIME Fall Meeting, Orlando, FL, Oct. 6-7, 1986, p. 135.

24. F. A. Shunk, Constitution of Binary Alloys, Second Supplement, McGraw-Hill, New York, 1969.

25. M. Hansen, Constitution of Binary Alloys, McGraw-Hill, New York, 1958.

26. M. J. Graham, J. I. Eldridge, D. F. Mitchell, and R. J. Hussey, Anion Transport in Growing Cr_2O_3 and Al_2O_3 Scales, Mater. Sci. Forum, 43, 207, 1989.

Distribution for ANL/FE–92/1

Internal:

S. Borys
H. Drucker
W. A. Ellingson
T. F. Kassner
C. A. Malefyt (2)
K. Natesan (10)
J.–H. Park (5)
D. Schmalzer
W. J. Shack
C. E. Till
R. W. Weeks
ANL Patent Dept.
ANL Contract File
TIS Files (3)

External:

DOE-OSTI, for distribution per UC-114 (35)
ANL Libraries

DOE Chicago Operations Office:
Manager F. Herbaty D. L. Bray

Materials and Components Technology Division Review Committee:
H. Berger, Industrial Quality, Inc., Gaithersburg, MD
M. S. Dresselhaus, Massachusetts Institute of Technology, Cambridge, MA
S. J. Green, Electric Power Research Institute, Palo Alto, CA
R. A. Greenkorn, Purdue University, West Lafayette, IN
C.–Y. Li, Cornell University, Ithaca, NY
P. G. Shewmon, Ohio State University, Columbus, OH
R. E. Smith, Electric Power Research Institute, NDE Ctr., Charlotte, NC

U.S. Department of Energy, Washington:
Office of Fossil Energy:
D. J. Beecy J. P. Carr H. Feibus C. W. Garrett
F. Glaser P. Muchunas G. Rudins T. B. Simpson
Office of Conservation:
J. J. Brogan A. A. Chesnes J. J. Eberhardt
J. Eustis E. W. Gregory II M. E. Gunn, Jr.
Basic Energy Sciences, Materials Science Division:
J.B. Darby

DOE Morgantown Energy Technology Center:
Director J. E. Notestein

DOE Oak Ridge Operations Office:
Manager E. E. Hoffman

DOE Pittsburgh Energy Technology Center:
Director J. D. Hickerson F. W. Steffen

Oak Ridge National Laboratory:
R. R. Judkins N. Cole J. H. DeVan

Other Government - University - Industry:

S. J. Dapkunas, National Institute of Standards and Technology, Gaithersburg, MD
D. Doughty, Sandia National Laboratories, Albuquerque, NM
D. W. Keefer, EG&G IDAHO, Inc., Idaho National Engineering Laboratory, Idaho Falls, ID
F. S. Pettit, University of Pittsburgh, Dept. of Materials Science and Engineering, Pittsburgh, PA
K. M. Prewo, United Technologies Research Center, East Hartford, CT
A. Schwarzkopf, National Science Foundation, Washington, DC
R. M. Spriggs, National Research Council, Washington, DC
I. G. Wright, Battelle Columbus Laboratories, Columbus, OH
K. M. Zwilsky, National Materials Advisory Board, National Research Council, Washington, DC

DATE
FILMED
8/25/92